Photoproduction of K_S Pairs at GlueX
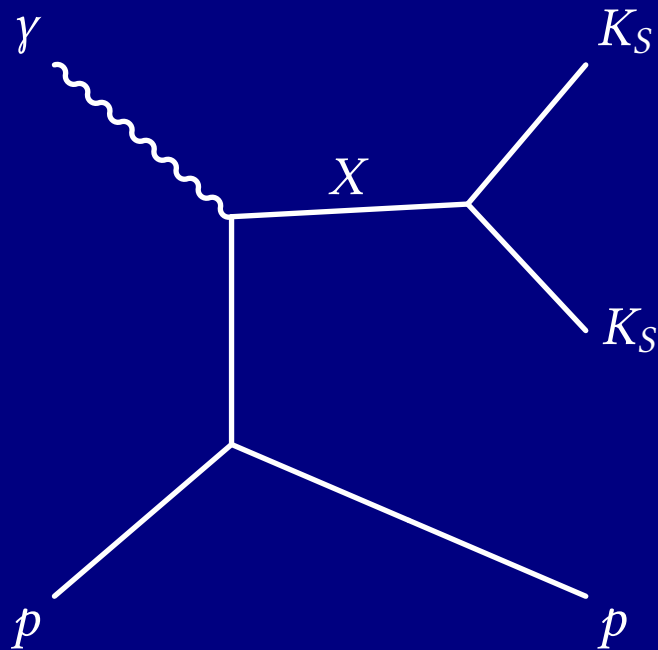
Nathaniel Dene Hoffman

Carnegie Mellon University

Table of Contents

Chapter 1

Introduction

1.1   A Brief History of Particle Physics

Since the days of the ancient Greeks, scientists and philosophers alike have been interested in the fundamental question concerning the composition of the universe. While some Greeks maintained that the world was composed of four indivisible elemental substances (fire, earth, air, and water) [1], this was at best a guess by the early philosophers, who had no mechanism with which to test their theory. Ironically, these philosophers struggled with a question to which us modern physicists still have no answer: Are the building blocks of the natural world fundamental (indivisible) [2]?

In 1808, John Dalton published a manuscript which described what is now called the "law of multiple proportions" after compiling several observations on chemical reactions which occur with specific proportions of their reactants. He anglicized the Greek *atomos*, meaning "not able to be cut", into the word we are familiar with—"atom" [3]. Towards the end of the century, J. J. Thomson demonstrated that cathode rays could be deflected by an electromagnetic field, an observation which could not be explained by the prevailing theory that the rays were some form of light [4]. Instead, he proposed that these rays were made up of charged particles he called "corpuscles" (later renamed to the familiar "electrons") [5]. Around the same time (between 1906 and 1913), Ernest Rutherford, Hans Geiger, and Ernest Marsden conducted experiments in which they scattered alpha particles through a thin metal foil, and, through an analysis of the scattering angles, concluded that a positively charged nucleus must exist at the center of atoms, surrounded by electrons [6].

Over the next several decades, the nucleus was further divided into protons and neutrons[1] [7], [8]. In 1964, Murray Gell-Mann and George Zweig proposed a theory that protons and neutrons (and all other baryons and mesons) were in fact composed of smaller particles Gell-Mann called "quarks" [9]. These particles, along with the

---

[1]For the discovery of the electron and neutron, Thomson and James Chadwick won Nobel Prizes in Physics in 1906 and 1935, respectively. Rutherford won the 1908 Nobel Prize in Chemistry for his research in radiation. However, I want to emphasize that while I mention the "big names" here, there are many who contributed in relative obscurity.

electron-like family of leptons (including neutrinos), the gauge bosons, and the Higgs boson, discovered in 2012 [10], comprise elements of the Standard Model, a mathematical model which describes all the known forces and matter of the universe, with the notable exceptions (at time of writing) of gravity, dark matter, dark energy, and neutrino masses.

This thesis begins at a time when physicists are working hard to find gaps in this model, mostly by probing higher and higher ranges of energy. The experimental work being done at GlueX, however, resides in a lower energy regime, which we usually describe as "medium energy physics". As I will elucidate later in this manuscript, the strong force is non-perturbative in this regime, making direct calculations through the Standard Model all but impossible. However, since the advent of Lattice Quantum Chromodynamics (LQCD) in 1974 [11], physicists have been able to make approximate predictions via computer simulations of the theory.

1.2   Thesis Overview

Herein, I will focus on a particular portion of the Standard Model that dictates the strong interaction, viz. interactions between quarks and gluons, the mediating gauge boson of the strong force. Beginning with a discussion of the theory and history of K_S (K-short) pair production in prior experiments, I will give a brief overview of the GlueX experiment. I will then outline some of the theoretical underpinnings and implications of glueballs to persuade the reader of the importance of this production channel in the larger scheme of GlueX.

Next, I will describe my own analysis, beginning with the the impetus of this study, a search for Σ^+ baryons using a different recombination of the final state in this channel. We will then turn our attention to the many resonances which decay to K_S pairs, and I will delineate the layers of data selection which have been carried out to produce a clean sample of events.

I will then discuss the process of partial-wave analysis (PWA), modeling resonances, and selecting a waveset for my data. I will conclude with the results from fits of these models to the data, the implications of such fits, and the next steps which I or another particle physicist might take in order to illuminate another corner of the light mesonic spectrum.

1.3   Motivation

While this will be discussed in detail later, I believe it is important to emphasize the motivation for such a study of photoproduction of $K_S K_S$. While the majority of GlueX research concerns the search for hybrid mesons (mesons with valence gluons which contribute to their angular momentum, including "exotic" mesons with quantum numbers forbidden by $q\bar{q}$-only states), such mesons cannot be found in this channel. Given a bound state of two spin-$\frac{1}{2}$ quarks with relative angular momentum L, total spin S and total angular momentum J (the eigenvalue of $\hat{J}^2 = \hat{L}^2 \oplus \hat{S}^2$), we

can define the parity operator $\hat{P}$ by its effect on the wave function of the system,

$$\hat{P}|\vec{r}\rangle = \eta|\vec{r}\rangle \tag{1.1}$$

where η can be determined by noting that states of angular momentum are generally proportional to a spherical harmonic in their angular distribution ($|r, \theta, \varphi; LM\rangle \sim Y_L^M(\theta, \varphi)$) and

$$\hat{P}Y_L^M(\theta, \varphi) = Y_L^M(\pi - \theta, \pi + \varphi) = (-1)^L Y_L^M(\theta, \varphi) \tag{1.2}$$

so $\eta = (-1)^L$. The Dirac equation can be used to show that the intrinsic parity of quarks and antiquarks, when multiplied, yields a factor of -1, so

$$\hat{P}|q\bar{q}; JLMS\rangle = -(-1)^L \tag{1.3}$$

Similarly, the charge-conjugation operator $\hat{C}$ (also called C-parity) will introduce a factor of $(-1)^L$ because exchanging charges of a (neutral[2]) quark-antiquark system is akin to reversing their positions under parity. If $|S\rangle$ is antisymmetric under C-parity, we should get an additional factor of -1, which is the case for the $S = 0$ singlet. With the aforementioned -1 due to the intrinsic parity of the quarks and antiquarks, we find

$$\hat{C}|q\bar{q}; JLMS\rangle = (-1)^{L+S} \tag{1.4}$$

Labeling states with the common J^{PC} notation, it can then be shown that states like 0^{--}, 0^{+-}, 1^{-+}, and 2^{+-} (among others) are not allowed states for $q\bar{q}$ mesons. As mentioned, the search for such states is a main focus of the GlueX experiment. However, since the particles we are concerned with decays to two identical mesons (K_S) which have a symmetric spatial wave function, and because these particles are mesons which follow Bose-Einstein statistics, the angular part of the total wave function must also be symmetric, i.e. J = even integers. Furthermore, because parity is conserved in strong decays, and the state of two identical particles is symmetric under parity, the decaying mesons must also have $P = +$. Finally, the strong interaction also conserves C-parity, and both kaons are neutral, so we can determine the J^{PC} quantum numbers of the resonance to be even^{++}. There should be no overlap here with the aforementioned exotic mesons, but that does not mean the channel is not of interest to GlueX and the larger scientific community. Particularly, the lowest lying glueball states are predicted to not only share these quantum numbers, but exist in the middle of the mass range produced by GlueX energies [12]. To add to this, the spin-0 isospin-0 light flavorless mesons, denoted as f_0-mesons, may be supernumerary, either due to mixing with a supposed light scalar glueball or by the presence of a light tetraquark or hybrid states (or both) [13].

However, it would be an understatement to say that the $K_S K_S$ channel at GlueX is not the ideal place to be looking for hybrids, glueballs or tetraquarks. This is because, while we have excellent handles for reconstructing

---

[2]For $\hat{C}$ to be Hermitian, and thus observable, acting it twice on a state should return the original state, so only eigenvalues of ± 1 are allowed. Therefore, only states which are overall charge neutral are eigenstates of $\hat{C}$.

this channel, we have no ability to separate particles of different isospin with these data alone. This means that these f states will be indistinguishable from their isospin-1 partners, the a-mesons. At first glance, it might seem like a model of the masses of these particles would make it easy to separate them, even if they remained indistinguishable between resonant peaks, but with broad states like the $f_0(1370)$ and states which sit right on top of each other (like the $f_0(980)$ and $a_0(980)$, which also tend to interfere with each other), there is likely no unique mass model which can distinguish all of the possible states without relying on data from other channels.

The silver lining is that, due to the GlueX detector's state-of-the-art angular acceptance [14], we do stand a chance at separating spin-0 states from spin-2 states, and GlueX's polarized beam allows us to further understand the mechanisms at play by giving us some indication of the parity of the t-channel exchanged particle in the production interaction. We can also use this channel as a proving ground for more complex amplitude analysis involving a mass model, which could be extended to a coupled-channel analysis in the future.

1.4   Past Analyses

The present work is certainly not the first attempt to study K_S^0 pair production. The earliest published experiment with a similar final state dates back to 1961, where researchers at CERN measured 54 events which ended in a final state which included two neutral kaons[3]. For the majority of the 1960s and 1970s, research into this final state was dominated by pion beam production off a proton target, aside from one kaon beam experiment in 1977 (see Table 1.1). In the 1980s, several collaborations at DESY began studying electron-positron collisions, which imply an internal virtual photon fusion as the production mechanism. These experiments are an important counterpoint to those involving hadrons, since the glueball does not couple to photons, so any intermediate glueball production in these reactions should be heavily suppressed [15], although radial excitations of any glueballs should couple [16]. While the statistical power of these experiments was very small at first (relative to pion beam experiments), the L3 collaboration at LEP and Belle at KEKB provided larger data samples in the first two decades of the 2000s. Until this study, ITEP and BNL held the statistical lead in non-photon-fusion experiments, and we now present a dataset which is larger than both, even using the most restrictive selections of data.

There has only been one prior experiment, published by the CLAS collaboration in 2018 [17], which used photoproduction as a means of accessing this channel. While the "golden channel" for glueball production remains radiative J/ψ decays to $K_S^0 K_S^0 \gamma$, since non-glueball intermediate processes converting charm quarks into strange quarks are suppressed, photoproduction could be effective at creating exotic hybrid states as well as glueballs via the photon's hadronic component or Pomeron exchange [16]. Additionally, the CLAS experiment did not utilize the polarized photon beam capability at JLab, but the current analysis at GlueX does, and this access to linear photon

---

[3]Since only K_S^0 eigenstates decayed inside the bubble chamber, while the longer lived K_L^0 would typically decay somewhere outside the chamber, these experiments infered a final state of $K_S^0 K_S^0$. The same can be said for modern experiments, including GlueX.

Channel	Collaboration	# Events	Year
$\pi^- p \to K_S^0 K_S^0 n$	CERN/PS	54	1961 [18]
$\pi^- p \to K_S^0 K_S^0 n$	BNL	19	1962 [19]
$\pi^- p \to K_S^0 K_S^0 n$	LRL	66	1962 [20]
$\pi^- p \to K_S^0 K_S^0$ + neutrals	BNL	374	1966 [21]
$\pi^- p \to K_S^0 K_S^0 n$	LRL	426	1966 [22]
$\pi^- p \to K_S^0 K_S^0 n$	LRL	418	1967 [23]
$\pi^- p \to K_S^0 K_S^0 n$	CERN/PS	2559	1967 [24]
$\pi^- p \to K_S^0 K_S^0 n$	ANL/ZGS	1969	1968 [25] & 1969 [26]
$\pi^- p \to K_S^0 K_S^0 n$	CERN/PS	4820	1975 [27]
$\pi^- p \to K_S^0 K_S^0 n$	CERN/PS	6380	1976 [28]
$\pi^- p \to K_S^0 K_S^0 n$	ANL/ZGS	5096	1976 [29] & 1979 [30]
$K^- p \to K_S^0 K_S^0$ + neutrals	CERN/PS	410	1977 [31]
$\pi^- p \to K_S^0 K_S^0 n$	BNL/MPS	1278	1980 [32]
$\pi^- p \to K_S^0 K_S^0 n$	BNL/MPS	29381	1982 [33]
$e^+ e^- \to e^+ e^- K_S^0 K_S^0$	DESY/TASSO	100	1983 [34]
???	???	???	1986 (Bolonkin)
???	???	???	1986 (Baloshin)
$\pi^- p \to K_S^0 K_S^0 n$	BNL/MPSII	40494	1986 [35]
$e^+ e^- \to e^+ e^- K_S^0 K_S^0$	DESY/PLUTO	21	1987 [36]
$K^- p \to K_S^0 K_S^0 \Lambda$	SLAC/LASS	441	1988 [37]
$e^+ e^- \to e^+ e^- K_S^0 K_S^0$	DESY/CELLO	26	1988 [38]
$e^+ e^- \to e^+ e^- K_S^0 K_S^0$	LEP/L3	62	1995 [39]
$p p \to p p K_S^0 K_S^0$	Fermilab/E690	11182	1998 [40]
$\pi^- p \to K_S^0 K_S^0$ + neutrals	ITEP	1000†	1999 [41]
$e^+ e^- \to e^+ e^- K_S^0 K_S^0$	LEP/L3	802	2001 [15]
$\pi^- C \to K_S^0 K_S^0 + X$	ITEP	553	2003 [42]
$e^+ e^- \to e^+ e^- K_S^0 K_S^0$	LEP/L3	870	2006 [43]
$\pi^- p \to K_S^0 K_S^0 n$	ITEP	40553	2006 [44]
$e^+ e^- \to e^+ e^- K_S^0 K_S^0$	KEKB/Belle	???‡	2013 [45]
$\gamma p \to K_S^0 K_S^0 p$	JLAB/CLAS	13500†	2018 [17]
$\gamma p \to K_S^0 K_S^0 p$	JLAB/GlueX	65468*	2025 (this analysis)

Table 1.1: Summary of all (known) past analyses involving production of K_S^0 pairs. Note that this is possibly not exhaustive and does not include any studies which focus on decays of an intermediate state, i.e. $J/\psi \to \gamma K_S^0 K_S^0$.

$\dagger$ - Estimated from plots.

$\ddagger$ - Reported as three orders of magnitude larger than LEP's result from 2006, but an exact count was difficult to estimate.

$*$ - Weighted number of events with KinFit $\chi_\nu^2 < 3.0$, the most restrictive selection used in this analysis (see Sections 2.1 and 2.2).

polarization can inform us of the parity exchanged in production of such exotic states. Our dataset is at least 4.8×

larger than what was used in the CLAS measurement.

Chapter 2

Experimental Design and Data Selection

2.1 The GlueX Experiment

GlueX, short for the Gluonic Excitation experiment located at the Thomas Jefferson National Accelerator Facility (JLab), first began collecting publication-quality data in 2016 with the goal of establishing the spectrum of light mesonic states including hybrid mesons and glueballs.

GlueX receives an unpolarized electron beam from the Continuous Electron Beam Accelerator Facility (CEBAF), which is then converted to linearly polarized photons via coherent bremsstrahlung from a diamond radiator (see Figure 2.1). The scattering electrons are detected in an array of high-resolution scintillators called the Tagger Mi-
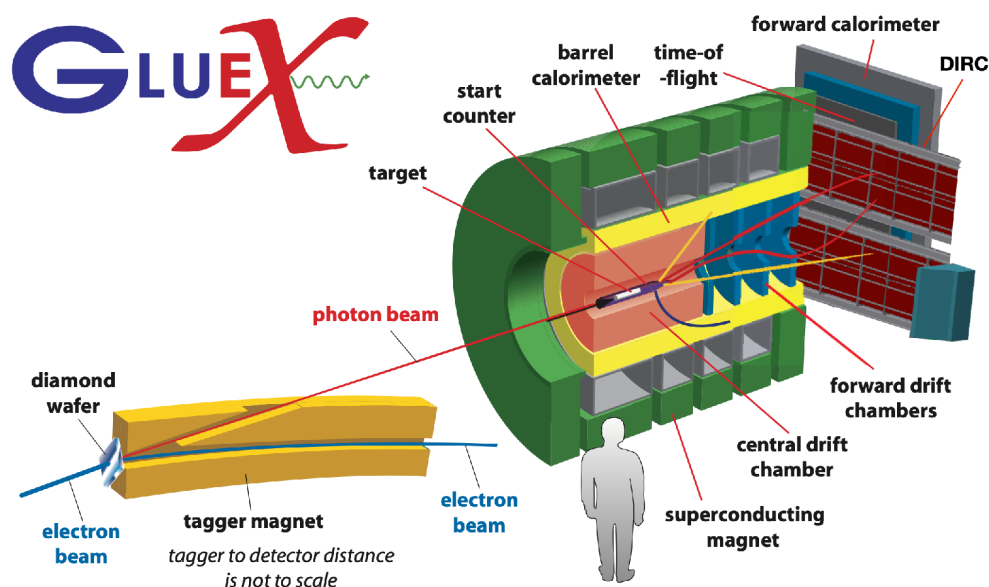

Figure 2.1: A diagram of the GlueX detector at JLab. The DIRC detector was installed in 2019 and was only present for about half of the data analyzed in this study.CITE
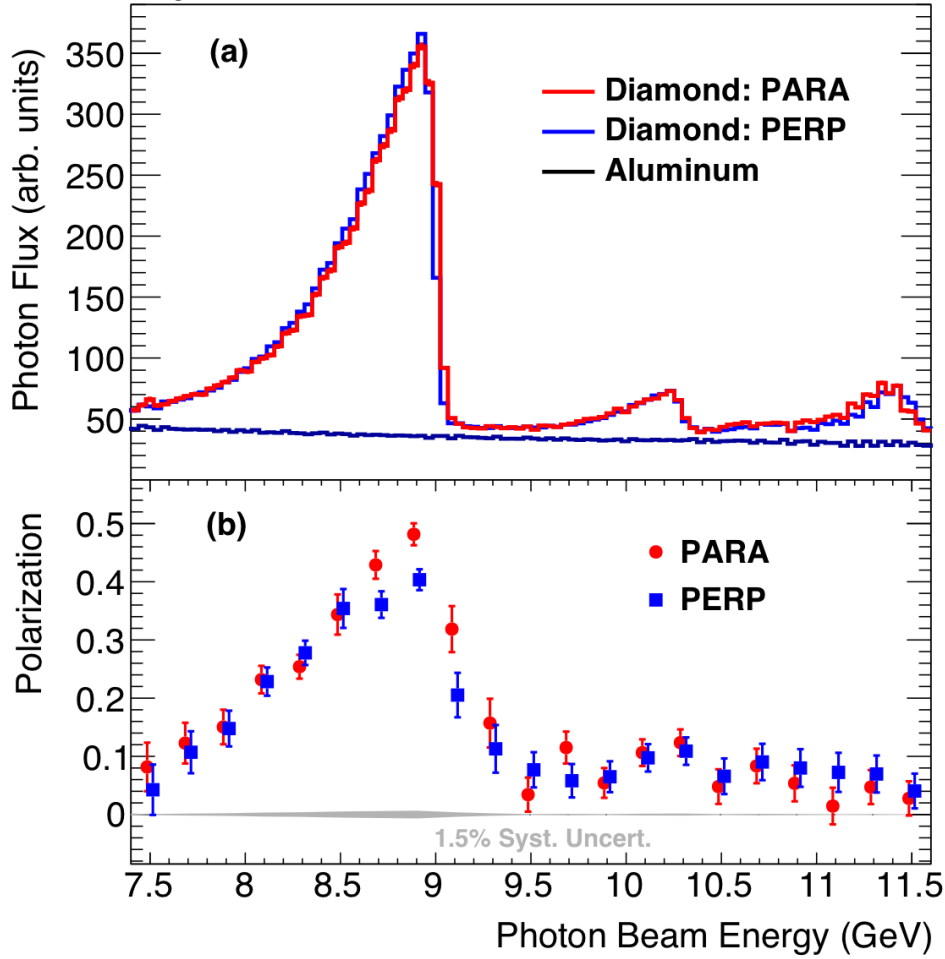
7

Figure 2.2: (a) Collimated photon beam intensity versus energy as measured by the Pair Spectrometer. (b) Collimated photon beam polarization as a function of beam energy, as measured by the Triplet Polarimeter, with data points offset horizontally by ±0.015 GeV for clarity. The labels PARA and PERP refer to orientations of the diamond radiator that result in polarization planes that are parallel and perpendicular to the horizontal, respectively (figure and caption from [14]).

croscope (TAGM) which covers beam energies between 8 and 9 GeV, a region of energy referred to as the "coherent peak". The orientation of the diamond radiator is optimized to produce the highest photon polarization and flux in this region (see Figure 2.2). The rest of the energy range, regions from about 3–8 GeV and 9–12 GeV, are covered by the lower-resolution Tagger Hodoscope (TAGH). These elements are used to determine only the photon energy, which is equal to the difference between the incident and outgoing electron energies [14].

To measure the polarization properties of the photon beam as well as the photon flux, the photon beam passes through a thin beryllium foil which induces e^+e^- pair production on some known fraction of the photons (see Figure 2.3). The angular distribution of the produced electrons along with an electron knocked out of the foil medium as part of the pair production process is measured by the Triplet Polarimeter (TPOL) to determine the photon polarization fraction. The Pair Spectrometer (PS) then counts the pair-produced electrons in coincidence with the TAGM
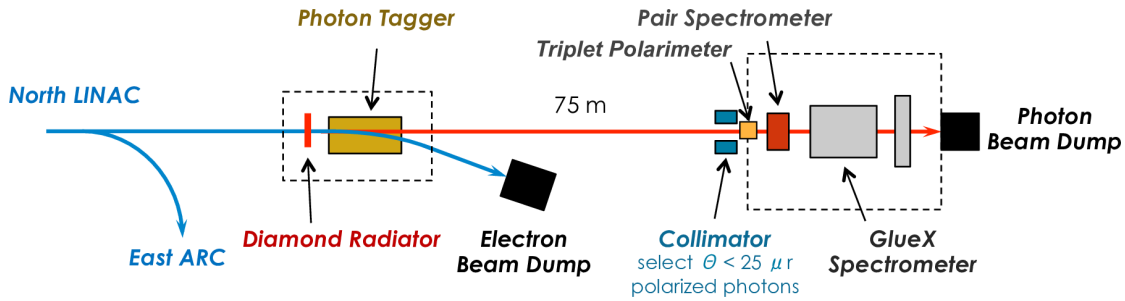
Figure 2.3: A diagram of the beamline layout of the Triplet Polarimeter (TPOL) and Pair Spectrometer (PS) used to measure the polarization and beam flux.

and TAGH detectors. A known fraction[1] of the beam is converted to e^+e^- pairs in this way, allowing for an accurate measurement of the photon flux and the energy dependence of the polarization fraction.

Photons which do not pair-produce in the beryllium radiator interact with a liquid hydrogen cryotarget, which maintains a temperature of 20.1 K, allowing the contents to act as a stationary proton target. A set of thin scintillators called the Start Counter (ST) surrounds the target, which captures the initial signals (and azimuthal angles) from reaction products and associates them with the electron radio frequency (RF) beam bunch from which the reaction originated[2]. Any products of the reaction next pass through either the Central Drift Chamber (CDC) or Forward Drift Chamber (FDC) depending on their trajectory (particles within $1°-10°$ of the beamline pass through the FDC, and the detector has partial coverage up to $20°$). The CDC is filled with long metal tubes at various orientations, while the FDC chambers are flat disks. Each tube/disk is filled with a gaseous mixture of argon and carbon dioxide[3] with a thin wire running through their center of each tube and an array of wires crossing the plane of each disk. The wire and tube/disk faces are held at a voltage differential, and charged particles passing through the chambers ionize the gases inside. The faster-moving electrons move towards the positively charged wires, while the slower-moving ions move towards the tubes/disks. The combination of these signals allows for the reconstruction of the trajectories of each charged particle which passes through each chamber. Both detectors are situated inside a solenoid with a

---

[1]We know the radiation length of the beryllium foil, and this along with the radiator thickness determines the fraction of photons which will pass through without interacting.

[2]The electron beam bunches from the CEBAF arrive every 4 ns, a rate of 250 MHz.

[3]These particular gases and the mixture ratio are chosen to reduce interfering effects from the magnetic field of the main solenoid.

Experiment	Run Period	Luminosity	Coherent Peak Range	Luminosity in Coherent Peak
Phase-I	Spring 2017	$74.7\,\text{pb}^{-1}$	8.2–8.8 GeV	$21.8\,\text{pb}^{-1}$
	Spring 2018	$223.8\,\text{pb}^{-1}$	8.2–8.8 GeV	$63.0\,\text{pb}^{-1}$
	Fall 2018	$141.1\,\text{pb}^{-1}$	8.2–8.8 GeV	$40.1\,\text{pb}^{-1}$
Phase-II	Spring 2020	$386.2\,\text{pb}^{-1}$	8.0–8.6 GeV	$132.4\,\text{pb}^{-1}$
Total		$825.8\,\text{pb}^{-1}$		$257.3\,\text{pb}^{-1}$

Table 2.1: Summary of total luminosity and total luminosity in the coherent peak for each run period.

magnetic field around 2 T, and this field bends the trajectories of charged particles, allowing for proper identification of the sign of the charge as well as the particle's momentum.

The Barrel Calorimeter (BCAL) surrounding the CDC and the Forward Calorimeter (FCAL) in front of the FDC measure the energy of electromagnetic deposits from interactions with charged and neutral particles. This includes photons originating from the decays of light neutral mesons like the π^0 and η. Because such neutral particles pass through the CDC and FDC without detection, these calorimeters are necessary for their reconstruction. However, since there are no intermediate trajectories, GlueX is unable to reconstruct the decay vertices of these neutral particles. Since we are studying a reaction with a fully charged final state, this might not seem important. However, in Section 2.3, we will discuss the study of neutral decays of $K_S^0 \to 2\pi^0 \to 4\gamma$, where the reconstruction will be severely limited due to the inability to reconstruct the decay vertex of the K_S^0.

There is a final scintillator array called the Time-of-Flight (TOF) detector situated immediately between the FDC and the FCAL. In combination with the ST and the RF timing information from the accelerator, this aids in charged-particle identification via a measurement of the flight time between the two detectors. Additionally, in 2019, an additional detector, the DIRC[4] detector was installed between the TOF and FDC to further aid in identification of charged pions and kaons. This detector measures the angle of the cone of Cherenkov radiation emitted by relativistic charged particles, which can be used to ascertain their velocity via the relation $\cos\theta_c \sim 1/v$. When compared to measurements of the particle's momentum, this detector can be used to distinguish pions, kaons, and protons. Further information about the GlueX detector and the DIRC can be found in references [14] and [46] respectively.

The data analyzed in this thesis were collected in four separate "run periods" across two experiment "phases", denoted Phase-I and Phase-II. Phase-I consists of three run periods, notated Spring 2017, Spring 2018, and Fall 2018 by the season and year when data collection began, and Phase-II contains one run period, Spring 2020[5] and is the only dataset which was collected after the DIRC installation. The total luminosity, coherent peak range, and luminosity in the coherent peak for each run period is listed in Table 2.1.

The entire GlueX detector has been simulated with Geant4. Due to small changes and updates to the detector

---

[4]An acronym for Detection of Internally Reflected Cherenkov light
[5]This run technically began at the end of 2019

and its simulation between run periods, we will treat these datasets separately during the analysis, only presenting combined results in summary. Therefore, when generating Monte Carlo simulated data to model detector acceptance, each run period must be simulated separately.

Particle Identification and the GlueX Kinematic Fit

Data collected from the GlueX detector mostly contains reaction topologies (the set of initial-, intermediate-, and final-state particles) which are not the channel of interest in this thesis, as the GlueX experiment uses a broad trigger to collect data with a wide range of final states. Additionally, due to the unavoidable finite resolution of each detector, the measured quantities such as the momentum of each particle might not exactly align with physical expectations (such as four-momentum conservation). For these reasons, we need to filter the detected data to just events which match our desired topology and kinematically fit the observables such as particle masses, decay vertices, and four-momenta with constraints that enforce conservation laws and other properties of interest.

This process begins with particle reconstruction, where the raw detector data is transformed into charged particle tracks (from the drift chambers), electromagnetic showers (from the calorimeters), and timing data from the ST, TOF, and accelerator RF signal. Next, the charged tracks are matched up with their respective showers from the calorimeters, and the remaining showers are labeled as "neutral showers" originating from photons (or possibly neutral particles like neutrons). At this stage, no particle identification is assigned to the charged and neutral tracks. Track reconstruction is performed before data is "skimmed" (separated into final-state topologies) so that all GlueX datasets are processed in the same way. My own analysis and data selection happens after track reconstruction, particle identification cuts, and the kinematic fit, after which there are still many events which likely belong to backgrounds which make it through these steps.

Particle Identification Cuts

The next stage involves filtering through reconstructed tracks to find candidate events which match our topology. Timing cuts are applied to whichever detector gives the best timing information (the order being BCAL, TOF, FCAL, ST). By timing, we mean the difference between the time measured in the detector and the time of the RF beam bunch measured in the TAGH/TAGM. Each set of charged tracks is identified with each charged particle in the topology (events with too many or too few charged tracks are excluded). Each hypothetical identification is then subjected to cuts on the energy lost in the drift chambers or deposited in the calorimeters. Since there are no "missing" final-state particles (such as a neutron) in our reaction, an additional cut is made on the missing energy (the difference between the initial energy from the beam photon and the summed energy of the detected final-state particles). Finally, cuts are made on the invariant mass of some particles, as well as the TODO missing mass (squared) of the entire reaction (the

Particle	Selected Values	Unit	Detector
γ	$-1.5 \leq \Delta t_{\mathrm{RF}} \leq 1.5$	ns	BCAL
	$-2.5 \leq \Delta t_{\mathrm{RF}} \leq 2.5$	ns	FCAL
	$-0.1 \leq \mathrm{MM}^2 \leq 0.1$	$(\mathrm{GeV}/c^2)^2$	N/A
$\pi^{\pm}$	$-1.0 \leq \Delta t_{\mathrm{RF}} \leq 1.0$	ns	BCAL
	$-0.5 \leq \Delta t_{\mathrm{RF}} \leq 0.5$	ns	TOF
	$-2.0 \leq \Delta t_{\mathrm{RF}} \leq 2.0$	ns	FCAL
	$-2.5 \leq \Delta t_{\mathrm{RF}} \leq 2.5$	ns	ST
	$\frac{dE}{dx} < \exp\left[-7.0\|\vec{p}\| + 3.0\right] + 6.2$	keV/cm ($\frac{dE}{dx}$), GeV/c ($\|\vec{p}\|$)	CDC
	$-1.0 \leq \mathrm{MM}^2 \leq 1.0$	$(\mathrm{GeV}/c^2)^2$	N/A
p	$-1.0 \leq \Delta t_{\mathrm{RF}} \leq 1.0$	ns	BCAL
	$-0.6 \leq \Delta t_{\mathrm{RF}} \leq 0.6$	ns	TOF
	$-2.0 \leq \Delta t_{\mathrm{RF}} \leq 2.0$	ns	FCAL
	$-2.5 \leq \Delta t_{\mathrm{RF}} \leq 2.5$	ns	ST
	$\frac{dE}{dx} > \exp\left[-4.0\|\vec{p}\| + 2.25\right] + 1.0$	keV/cm ($\frac{dE}{dx}$), GeV/c ($\|\vec{p}\|$)	CDC
	$-0.5 \leq \mathrm{MM}^2 \leq 4.41$	$(\mathrm{GeV}/c^2)^2$	N/A
π^0	$0.08 \leq \mathrm{IM} \leq 0.19$	GeV/c^2	N/A
	$-1.0 \leq \mathrm{MM}^2 \leq 1.0$	$(\mathrm{GeV}/c^2)^2$	N/A
K_S^0	$0.3 \leq \mathrm{IM} \leq 0.7$	GeV/c^2	N/A
	$-1.0 \leq \mathrm{MM}^2 \leq 2.0$	$(\mathrm{GeV}/c^2)^2$	N/A
N/A	$-3.0 \leq \mathrm{ME} \leq 3.0$	GeV	N/A

Table 2.2: PID cuts used in event reconstruction. MM^2 corresponds to the missing mass squared, IM corresponds to the invariant mass, and *ME* corresponds to the total missing energy.

squared difference in invariant mass between the initial and final state). A summary of these particle identification (PID) cuts can be seen in Table 2.2.

Kinematic Fit

The final stage of reconstruction invokes a kinematic fit (KinFit) over data which has passed all separate PID cuts. The general structure of the kinematic fit is underpinned by the following derivation from [?][6]. This kinematic fit minimizes the following objective function:

$$\chi^2(\vec{\eta}, \vec{\xi}) = (\vec{y} - \vec{\eta})^{\mathsf{T}} \mathbf{V}_{\vec{y}}^{-1} (\vec{y} - \vec{\eta}) + 2\vec{\lambda}^{\mathsf{T}} \vec{f}(\vec{\eta}, \vec{\xi}) \tag{2.1}$$

where $\vec{y}$ are the experimentally measured values of observables $\vec{\eta}$, $\mathbf{V}_{\vec{y}}$ is the covariance matrix of the measured $\vec{y}$, $\vec{f}(\vec{\eta}, \vec{\xi}) = 0$ are constraints applied to the system with additional free parameters $\vec{\xi}$ (which do not correspond to measured observables), and λ are unknown Lagrange multipliers for said constraints. For example, $\vec{y}$ could include the measured four-momenta of all initial- and final-state particles, and $\mathbf{V}_{\vec{y}}$ would describe the uncertainty (from the detector elements) of each measurement. One possible constraint function $\vec{f}$ might minimize the difference between

---

[6]How to cite GlueX docdb 2112?

the initial and final four-momentum, as in Equation (2.12). Since we wish to minimize χ^2, we first take derivatives with respect to each set of free parameters,

$$\frac{\partial \chi^2}{\partial \vec{\eta}} = \mathbf{V}_{\vec{y}}^{-1}(\vec{\eta} - \vec{y}) + \left(\frac{\partial \vec{f}}{\partial \vec{\eta}} \right)^{\mathsf{T}} \vec{\lambda} \tag{2.2}$$

$$\frac{\partial \chi^2}{\partial \vec{\lambda}} = \vec{f}(\vec{\eta}, \vec{\xi}) \tag{2.3}$$

$$\frac{\partial \chi^2}{\partial \vec{\xi}} = \left(\frac{\partial \vec{f}}{\partial \vec{\xi}} \right)^{\mathsf{T}} \vec{\lambda} \tag{2.4}$$

To find an extremum, we set these each to $\vec{0}$ and solve. At GlueX, the KinFit uses the Newton-Raphson method. First, we Taylor expand the constraint equations to first order,

$$\vec{f}(\vec{\eta}, \vec{\xi}) \approx \vec{f}(\vec{\eta}_0, \vec{\xi}_0) + \left(\frac{\partial \vec{f}}{\partial \vec{\eta}} \right) \Big|_{\vec{\eta}_0, \vec{\xi}_0} (\vec{\eta} - \vec{\eta}_0) + \left(\frac{\partial \vec{f}}{\partial \vec{\xi}} \right) \Big|_{\vec{\eta}_0, \vec{\xi}_0} (\vec{\xi} - \vec{\xi}_0) \tag{2.5}$$

Assuming $\vec{\eta}_0$ and $\vec{\xi}_0$ are near the true minimum, we can set up an iterative method of approach,

$$\vec{f}_i + \left(\frac{\partial \vec{f}}{\partial \vec{\eta}} \right)_i (\vec{\eta}_{i+1} - \vec{\eta}_i) + \left(\frac{\partial \vec{f}}{\partial \vec{\xi}} \right)_i (\vec{\xi}_{i+1} - \vec{\xi}_i) = \vec{0} \tag{2.6}$$

where $\vec{f}_i \equiv \vec{f}(\vec{\eta}_i, \vec{\xi}_i)$, $\left(\frac{\partial \vec{f}}{\partial \vec{\eta}} \right)_i \equiv \left(\frac{\partial \vec{f}}{\partial \vec{\eta}} \right) \Big|_{\vec{\eta}_i, \vec{\xi}_i}$, and $\left(\frac{\partial \vec{f}}{\partial \vec{\xi}} \right)_i \equiv \left(\frac{\partial \vec{f}}{\partial \vec{\xi}} \right) \Big|_{\vec{\eta}_i, \vec{\xi}_i}$. To carry out an iteration, we need to determine the next step in each of the free directions $\vec{\eta}_{i+1}$ and $\vec{\xi}_{i+1}$. We start by writing the iterative forms of Equations (2.2) and (2.4) as

$$\mathbf{V}_{\vec{y}}^{-1}(\vec{\eta}_{i+1} - \vec{y}) + \left(\frac{\partial \vec{f}}{\partial \vec{\eta}} \right)_i^{\mathsf{T}} \vec{\lambda}_{i+1} = 0 \tag{2.7}$$

$$\left(\frac{\partial \vec{f}}{\partial \vec{\xi}} \right)_i^{\mathsf{T}} \vec{\lambda}_{i+1} = 0 \tag{2.8}$$

To obtain the next iterative estimate of $\vec{\eta}$ by rearranging Equation (2.7) as

$$\vec{\eta}_{i+1} = \vec{y} - \mathbf{V}_{\vec{y}} \left(\frac{\partial \vec{f}}{\partial \vec{\eta}} \right)_i^{\mathsf{T}} \vec{\lambda}_{i+1} \tag{2.9}$$

Inserting this back into Equation (2.6), we get

$$\vec{0} = \underbrace{\vec{f_i} + \left(\frac{\partial \vec{f}}{\partial \vec{\eta}}\right)_i (\vec{y} - \vec{\eta_i})}_{\vec{r_i}} - \underbrace{\left(\left(\frac{\partial \vec{f}}{\partial \vec{\eta}}\right)_i \mathbf{V}_{\vec{y}} \left(\frac{\partial \vec{f}}{\partial \vec{\eta}}\right)_i^{\mathsf{T}}\right)}_{\mathbf{S}_i} \vec{\lambda}_{i+1} + \left(\frac{\partial \vec{f}}{\partial \vec{\xi}}\right)_i \left(\vec{\xi}_{i+1} - \vec{\xi}_i\right)$$

$$\vec{0} = \vec{r_i} - \mathbf{S}_i \vec{\lambda}_{i+1} + \left(\frac{\partial \vec{f}}{\partial \vec{\xi}}\right)_i \left(\vec{\xi}_{i+1} - \vec{\xi}_i\right)$$

$$\vec{\lambda}_{i+1} = \mathbf{S}_i^{-1} \left(\vec{r_i} + \left(\frac{\partial \vec{f}}{\partial \vec{\xi}}\right)_i \left(\vec{\xi}_{i+1} - \vec{\xi}_i\right)\right) \tag{2.10}$$

We can plug this definition of $\vec{\lambda}_{i+1}$ into Equation (2.8) to find the iterative update for $\vec{\xi}$:

$$\vec{0} = \left(\frac{\partial \vec{f}}{\partial \vec{\xi}}\right)_i^{\mathsf{T}} \mathbf{S}_i^{-1} \vec{r_i} + \underbrace{\left(\frac{\partial \vec{f}}{\partial \vec{\xi}}\right)_i^{\mathsf{T}} \mathbf{S}_i^{-1} \left(\frac{\partial \vec{f}}{\partial \vec{\xi}}\right)_i}_{\mathbf{U}_i} \left(\vec{\xi}_{i+1} - \vec{\xi}_i\right)$$

$$\vec{\xi}_{i+1} = \vec{\xi}_i - \mathbf{U}_i^{-1} \left(\frac{\partial \vec{f}}{\partial \vec{\xi}}\right)_i^{\mathsf{T}} \mathbf{S}_i^{-1} \vec{r_i} \tag{2.11}$$

To perform the kinematic fit, we use the available measured observables and their covariances (contained in $\vec{r}$, $\mathbf{S}$, and $\mathbf{U}$) to update our estimate of $\vec{\xi}$ via Equation (2.11). Next, we use that result to update $\vec{\lambda}$ via Equation (2.10). Finally, we update $\vec{\eta}$ via Equation (2.9). This process is repeated until the desired precision of these variables is met, and is guaranteed to converge as long as the initial values start near the minimum. The χ^2 value obtained from evauating Equation (2.1) on the converged values tells us the quality of the fit. See Figure 2.4 for the distribution of $\chi^2_\nu \equiv \chi^2/\nu$, where ν is the number of degrees of freedom in the fit ($\nu = 11$ for this analysis), for both the real data and Monte Carlo simulation of the signal.

The constraints $\vec{f}$ used in this channel include four-momentum conservation,

$$\sum_{f\in\text{final}} p_f^\mu - \sum_{i\in\text{initial}} p_i^\mu = 0^\mu \tag{2.12}$$

where the sum over four-momenta of of the initial-state particles must match that of the final-state particles, and the masses of each intermediate K_S^0,

$$p_{K_S^0}^2 - m_{K_S^0}^2 = 0 \tag{2.13}$$

where $m_{K_S^0}$ is the known mass of the K_S^0 and $p_{K_S^0}$ is the fitted estimate of the four-momentum reconstructed from the $\pi^+\pi^-$ four-momentum measured by the detectors. Additionally we constrain the initial and final positional vertices of each production step in the topology. For this channel, this means we constrain the initial production vertex and the point of closest approach of the K_S^0s and recoil proton, as well as the decay vertex of each K_S^0 with
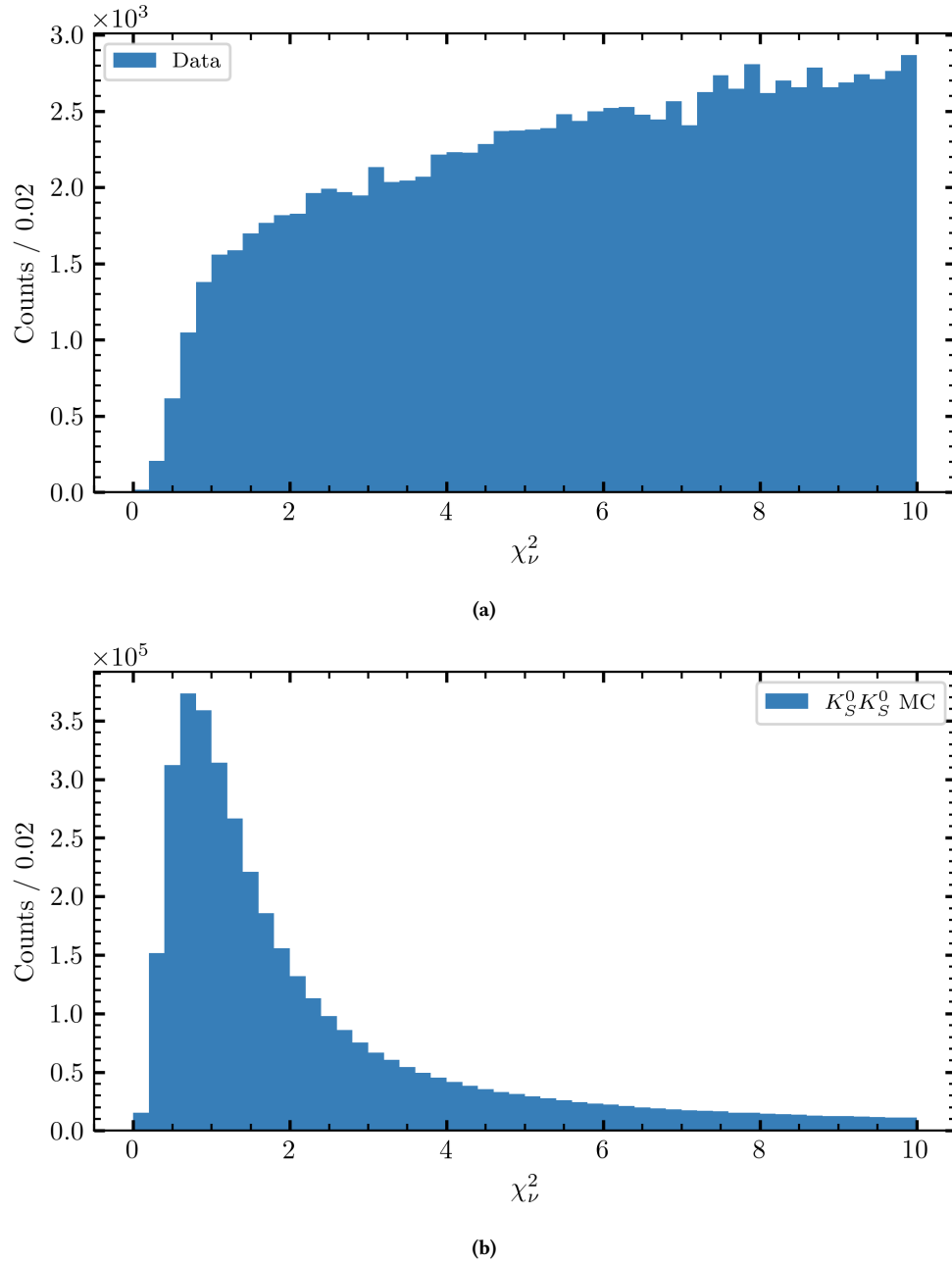
(a)

(b)

Figure 2.4: Distributions of χ_ν^2 (the χ^2 per degree of freedom of the GlueX kinematic fit) for (a) data and (b) signal Monte Carlo after reconstruction cuts but before any fiducial selections from Section 2.2. Note that the data extends past $\chi_\nu^2 > 10$, but the plot was truncated for legibility. Both datasets have had accidental subtraction applied and combos flattened (see Sections 2.1 to 2.2).

the closest approach of its constituent pions. It is important to note that this vertex constraint cannot be done in the case where a K_S^0 decays to $2\pi^0$, since the neutral pions will decay to 2γ which can only be detected without tracking in the calorimeters. Because there is not a second point of detection for these photons, their trajectory and therefore the point at which the original π^0 decayed is unknown, so there is no way to further reconstruct the kaon decay vertex because the point of closest approach is unknown[7]. Therefore, when we specify channels where one or both kaons decay as $K_S^0 \to 2\pi^0$, we do not include these K_S^0s in the kinematic fit at all, and must infer them by adding the π^0 four-momenta (see Section 2.3). For the main $\gamma p \to K_S^0 K_S^0 p \to 2\pi^+ 2\pi^- p$ channel, we have four constraints from four-momentum conservation, two mass constraints (one for each kaon), 14 vertex constraints (two for each constrained particle[8], viz. four pions, two kaons, and a proton), and nine unknowns from the vertex constraints (the position of the vertex introduces three unknowns for each vertex, and there are three constrained vertices, viz. two kaon decays and the initial production vertex). This gives a total of 20 constraints with nine unknowns, or 11 degrees of freedom in the fit.

Combos

While the initial interaction vertex in theory contains a single photon, in practice, the incident beam contains multiple tagged photons, any of which might provide the requisite energy needed to kinematically generate a given set of final-state tracks. Additionally, there could be multiple ways to recombine or identify final-state particles to arrive at the same event topology. The GlueX reconstruction process considers all valid combinations of tagged photons and sets of reconstructed final-state particles and saves each one in a sub-event called a "combo". Each event has at least one of these combos, and some events may have many due to there being many candidate beam photons with similar energies. Since only one combo can be the true event, we need to flatten the data in a way that avoids double counting events. The method for doing so is discussed in Section 2.2.

2.2 Data Selection for the $K_S K_S$ Channel

These reconstruction steps all take place before we interact with the data. The cut values in Table 2.2 are loose, and there is surely background remaining. To remove it, we first must know the potential sources of backgrounds in the $K_S^0 K_S^0$ channel, which we will do by simulating a large set of events with many different reaction topologies, passing them through reconstruction, and then comparing the distributions of each topology which makes it through. The simulation uses the bggen Monte Carlo generator, which in turn uses PYTHIA [47] for event generation and a

---

[7]The best we could do would be to assume the kaon decayed at the initial reaction vertex inside the target, which is not only unrealistic given that kaons decay via the weak interaction, but also causes problems later when we try to calculate the kaon lifetime to use in event weighting in Section 2.3.

[8]This is because we independently constrain the distance of a particle to the unknown vertex along two planes, the "bend" plane and the "non-bend" plane, named for being equal/perpendicular to the plane in which the trajectory of the particle is bending due to the magnetic field at the vertex point.
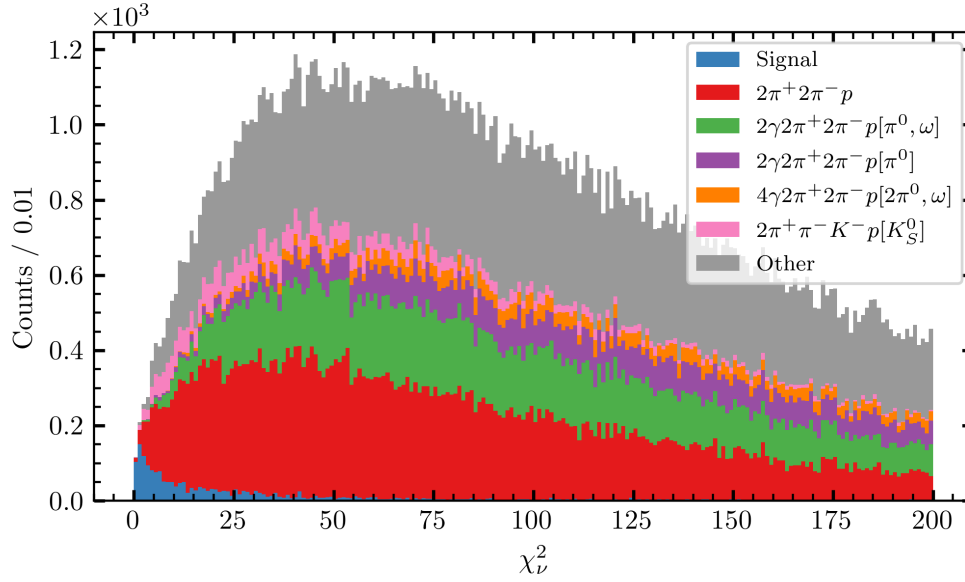
Figure 2.5: The reduced χ^2 statistic of the GlueX kinematic fit for the `bggen` simulation. The stacked histogram contains the signal channel, $K_S^0 K_S^0$ as well as the five most prominent background components.

GlueX implementation of `Geant4` [48], [49], [50]. The relative proportions of reaction topologies do not necessarily reflect the production cross sections we expect to see in data (for instance, there are no resonances included in the $K_S^0 K_S^0$ channel), but they should give us a good idea of the kinds of topologies which leak into this channel.

We will first look at the performance of the GlueX kinematic fit on `bggen` data in Figure 2.5. In this plot, we see the signal, which predictably peaks at $\chi^2_\nu \sim 1$, as well as several background topologies. These topologies are labeled by their final state along with any intermediate decaying resonances in square brackets. The top five potential backgrounds, in order of the size of their contribution after reconstruction, are as follows. First, $2\pi^+ 2\pi^- p$ shares the final state of the signal channel but does not contain any K_S^0 intermediate decays. Second, $2\gamma 2\pi^+ 2\pi^- p[\pi^0, \omega]$ contains an ω which decays to $\pi^+ \pi^- \pi^0$, followed by the π^0 decaying to 2γ. The addition of extra photons is common in these backgrounds, since missing the photon detections makes the final state identical to the signal. The next two reactions, $2\gamma 2\pi^+ 2\pi^- p[\pi^0]$ and $4\gamma 2\pi^+ 2\pi^- p[2\pi^0, \omega]$ both include an undetected π^0. Finally, $2\pi^+ \pi^- K^- p[K_S^0]$ contains a K^- which is mistakenly identified as a π^-.

It seems sensible to make a cut on the χ^2_ν of the kinematic fit, since the signal is clearly favored at lower values. Below $\chi^2_\nu < 10$, the background topologies are dominated by the 4π channel which does not contain kaons. As such, this source of background will be our primary focus for removal.
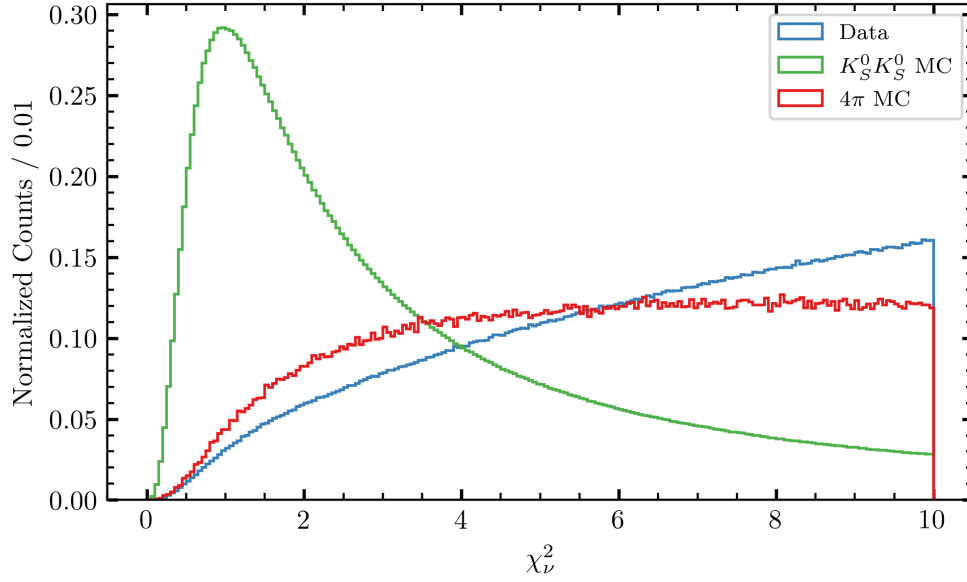
Figure 2.6: The normalized distributions of χ^2_ν for the true data and phase-space signal and 4π background Monte Carlo.

Fiducial Cuts

To get a clearer picture of the data, we will first make a loose cut selecting only events with $\chi^2_\nu < 10$. We can then generate phase-space Monte Carlo for the 4π background reaction and search for potential ways to separate it from the signal by comparing the distributions of common kinematic variables.

In Figure 2.6, we can see the various distributions of the data and each simulated channel. Unfortunately, the data distribution resembles the 4π background distribution much better than the signal Monte Carlo, but now we also know that the signal decays rapidly at higher values of χ^2_ν, so a tighter selection might improve the signal-to-background ratio, even if we cannot immediately see a peak in the data near unity. We can use the overall probability densities from the Monte Carlo simulations to inform our decision on where to place a cut. We begin by defining the true/false positive rates as

$$\text{TPR}(x_c) \equiv \epsilon_S(x_c) = \int_0^{x_c} \mathrm{d}x\, p_S(x) \tag{2.14}$$

$$\text{FPR}(x_c) \equiv \epsilon_B(x_c) = \int_0^{x_c} \mathrm{d}x\, p_B(x) \tag{2.15}$$

where $p_S(x)$ and $p_B(x)$ are the probability densities of the signal and background Monte Carlo, respectively, calculated from the normalized distributions over χ^2_ν detailed in Figure 2.6. The Youden J-statistic [51], [52] can be used as a criterion for finding the optimal cut value x_c [53], [54]. It relates the sensitivity (ϵ_S) and the specificity ($1 - \epsilon_B$) as
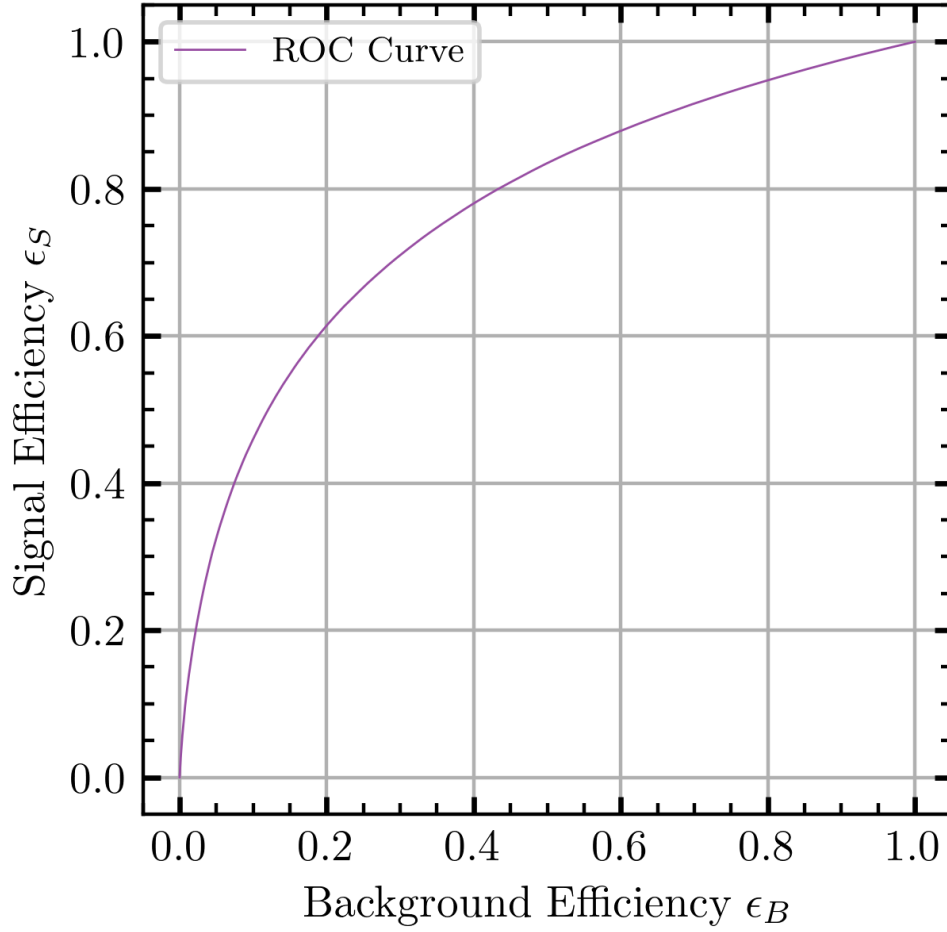
Figure 2.7: The receiver operating characteristic (ROC) curve for selections on χ^2_ν constructed from the signal and background Monte Carlo distributions.

$$J(x_c) = \epsilon_S(x_c) - \epsilon_B(x_c) \tag{2.16}$$

The Youden J-index is equivalent to the distance between the no-discrimination line and the receiver operating characteristic (ROC) curve shown in Figure 2.7. The Youden J-index is shown in Figure 2.8, and it is maximal at a value of $\chi^2_\nu = 3.4$. Therefore, we will use this value in our selection on χ^2_ν, although we will consider other values as well since we have other methods for separating the signal from the background (see Section 2.3).

Another common selection which can be made is on the squared missing mass of an event, which is just the square of the difference between the initial- and final-state four-momenta. This variable, visualized in Figure 2.9, predictably peaks at zero for the data, signal Monte Carlo, and background Monte Carlo, and the overall distributions for the signal and backgound simulated events are nearly identical. This indicates that a selection on this variable would not be very useful at distinguishing the signal from the background.
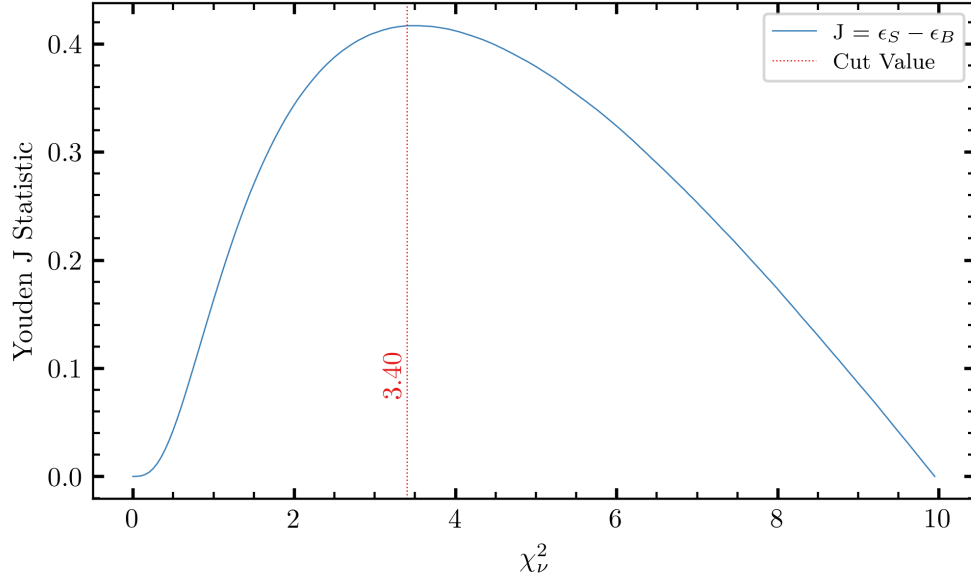
Figure 2.8: The Youden J-statistic for selections on χ^2_ν constructed from the signal and background Monte Carlo distributions. The maximal value indicates a selection at $\chi^2_\nu = 3.4$ would be the maximally informed decision boundary.
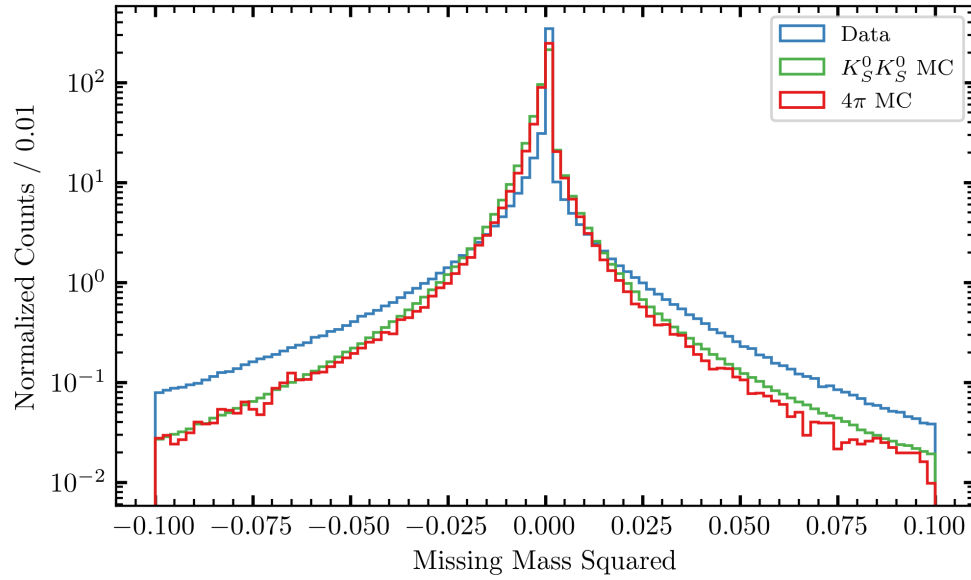

Figure 2.9: The normalized distributions of missing mass squared for the true data and phase-space signal and 4π background Monte Carlo.
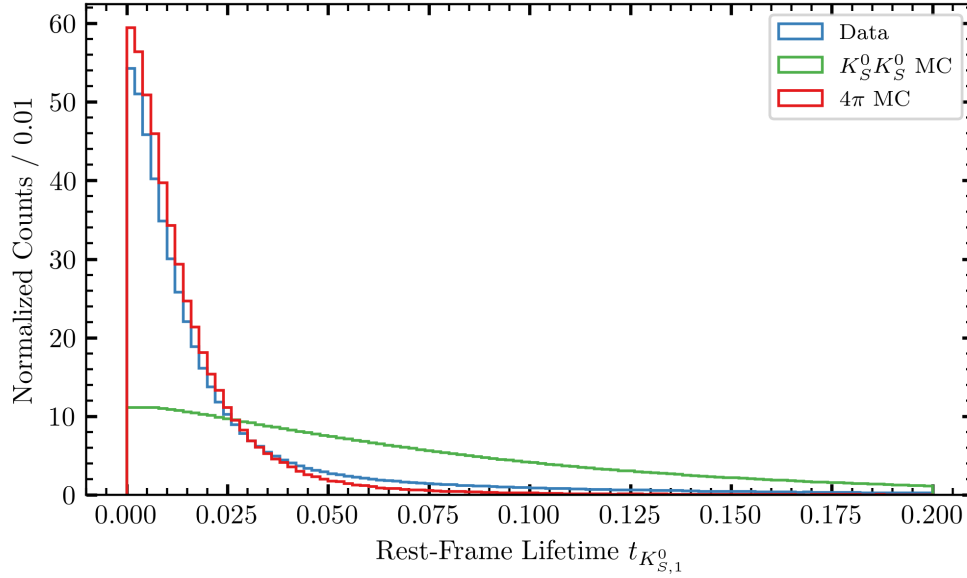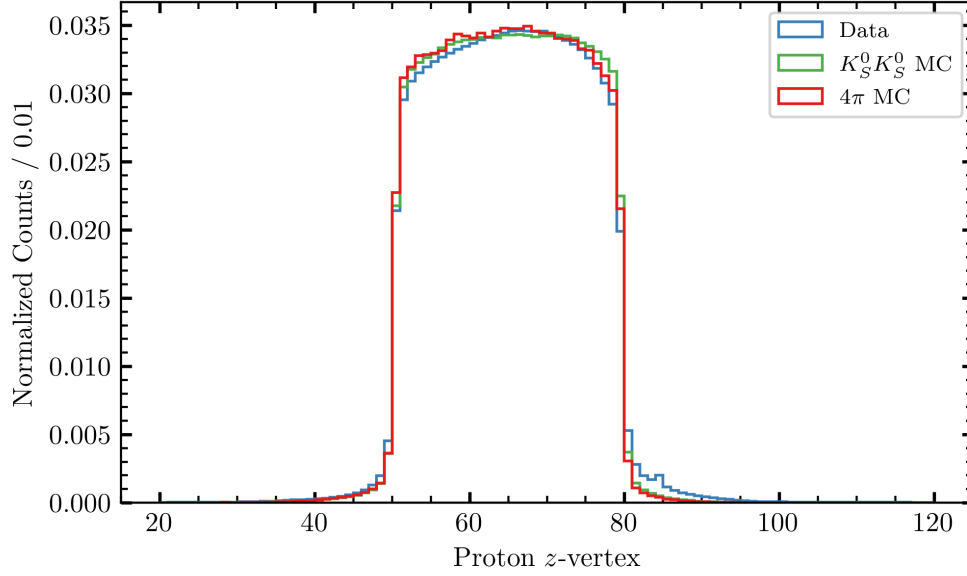
Figure 2.10: The normalized distributions of the rest-frame lifetime of one of the K_S^0 candidates for the true data and phase-space signal and 4π background Monte Carlo.

Recall that the main difference between the signal and background channels described here is the presence of decaying K_S^0 particles in the signal channel. These particles have a well-known lifetime around 89.54 ps due to their decay into non-strange mesons requiring a weak interaction. While we might not know the exact process which creates the 4π background, we can assume a strong interaction produces the pions, which should happen several orders of magnitude faster than the K_S^0 decay. Due to the resolution of the detector, we still expect these events to appear to have some non-zero distribution in rest-frame lifetime when we mistakenly interpret pairs of pions as kaons, but it will be vastly different from that of the signal.

We can see the effect of this in Figure 2.10. The exponential slope of the signal Monte Carlo is distinct from that of the background Monte Carlo, but the data distribution unfortunately seems to be dominated by this background. While we could use the Youden J-statistic again to determine a cut, largest portion of the true signal appears in the same place as the largest portion of background, and we would have to remove many good events just to get rid of the majority of the background. Rather than performing a hard cut on rest-frame lifetime, we will instead use statistical weighting methods described in Section 2.3.

Before we do this, however, there is one more minor selection which we will perform, which is a selection on the z-vertex of the target proton. We know the exact location of the target with respect to the detector, and we really only want to deal with events which we know originated inside this target. The distribution of the z-vertex values can be seen in Figure 2.11. We will select events with $50\,\text{cm} < z < 80\,\text{cm}$, as this is the known length and position of the target relative to the detector elements. While there is an indication of events in the signal Monte Carlo in

Variable	Selected Values
χ_ν^2	$\chi_\nu^2 < 3.4$
Target proton-z	$50\,\mathrm{cm} < z < 80\,\mathrm{cm}$

Table 2.3: Fiducial cuts performed after event reconstruction.

Figure 2.11: The normalized distributions of the target proton z-vertex for the true data and phase-space signal and 4π background Monte Carlo.

the regions which are removed, we know that while these events originated from the target, their z-vertex has been misidentified, so we should remove them anyway.

In total, we only have two main fiducial selections on the data, as illustrated in Table 2.3.

Accidental Subtraction

Before we can discuss subtracting the 4π background, we need to deal with another source of background which we cannot avoid with cuts. As mentioned in Section 2.1, each event in the dataset holds multiple "combos"—alternate hypotheses for the set or ordering of the particles which make up the topology. For example, in the $K_S^0 K_S^0$ final state, there are two identical π^+ and π^- particles. The choice of which π^+ goes with which π^- to form each kaon is partially constrained by th kinematic fit, but in the case where both pion combinations yield results which pass through the entire reconstruction and particle identification process, both are included as separate combos in the same event. The fiducial selections we performed in Section 2.2 eliminate many of these combos, since the incorrect combinations will sometimes have very high χ_ν^2, but there may be some remaining at the end of these selections. For this combinatoric case, we can reduce the effect of incorrect combinations by only selecting the combo with the

lowest χ_ν^2 in each event. While this does not guarantee that we will have the correct combination, it will prevent us from double-counting, and it is more likely that the best χ_ν^2 is the true event.

Additionally, we can get combos from different beam photon combinations. If multiple tagged photons have energies which are compatible with the reaction, each is included as a separate combo. It can also be the case that the true photon was simply not reconstructed, and some incorrect photon which was close enough was matched with the combo instead. In either case, we have multiple combos which do not correspond to their true beam events. We call both of these cases "accidental" combos. To account for this, we first recall that the accelerator produces beam bunches every 4 ns in radio-frequency (RF) bunches. A beam bunch consistent with a given event is labeled "in-time", while the surrounding bunches are called "out-of-time". We can reduce the impact of these accidental combos by estimating the contribution they have on the in-time events and using out-of-time events as a negatively-weighted background estimation. Since the in-time accidentals are indistinguishable from true events, we must use events which also pass through kinematic selections in our subtraction, and these out-of-time events are kinematically good events. The estimation of the scaling for these out-of-time contributions has been calculated via systematic studies of the various tagger components. For our data, we choose to include eight bunches of accidentals, although we cut out the nearest bunches to avoid using in-time events in our subtraction. The distribution of the difference in RF times with respect to the event time is shown in Figure 2.12. In this figure, the in-time events are located in the peak centered at zero, and we cut the peaks immediately on either side, and we define the boundaries between peaks using a peak width of 4 ns[9]. The remaining three out-of-time peaks on either side are given a negative weight (approximately 1/6th for each) while the in-time peak gets a weight of 1.

To unify this accidental subtraction with the combinatoric reduction done by selecting the best χ_ν^2, we first perform the χ_ν^2 selection, which will reduce each event to a single combo (some of which might be in the out-of-time peaks), and then we carry out the accidental subtraction. At this stage, the only background which remains unaccounted for is that of incorrect topologies disguised as our signal.

2.3   sPlot Weighting

At this stage in the analysis, we have no more simple cuts which can improve the signal-to-background ratio in the dataset, but we know there must still be background remaining, as is indicated by the excess events with small kaon rest-frame lifetimes seen in Figure 2.13. In this figure, we see that one of the intrinsic properties of a K_S^0, its well-known lifetime, is not distinct in the data. Rather, we seem to have at least two exponential slopes in the rest-frame lifetime distribution of each kaon, one which is close to what we see in signal Monte Carlo, and another which is similar to the 4π background Monte Carlo. We must now turn to more elaborate methods of separating the signal

---

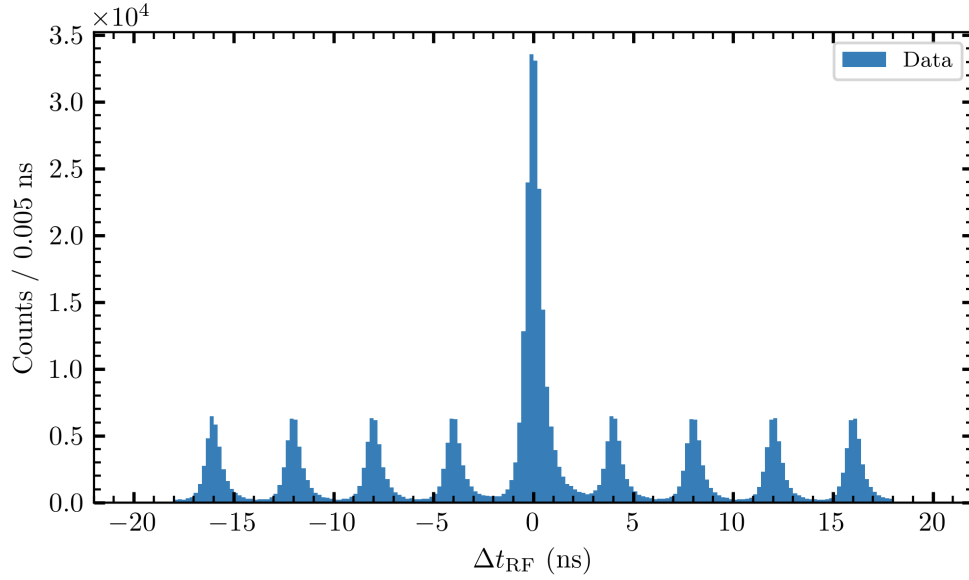[9]The exact value used is 4.008 016 032 ns.

Figure 2.12: The time difference between the RF time recorded by the tagger and the event time. The main peak in the middle contains in-time events while the four peaks on either side are the out-of-time events added to the dataset to simulate accidental combos in the main peak.

from this potential background seepage. The primary method we will use to do this is sPlot [55][10], a weighting scheme which corrects the naïve probabilistic weights one might first think to construct (dubbed "inPlot"). We begin by giving a basic explanation of inPlot before describing the sPlot correction.

For all of the statistical weighting methods which will be mentioned here, we need some model for the signal and background probability distribution functions (PDFs) for some "discriminating" variable. This variable is called "discriminating" because it the variable for which we know the shape of these distributions beforehand. The usual example is a "bump-on-a-background", in which the discriminating variable may be a mass distribution (m) where signal events show up as a peaking structure while background events are more uniformly distributed. In such situations, it is common to use the extremes of the mass distribution (sidebands) as estimates of the background everywhere, weighting these events negatively while the events in the peak are weighted positively (a sideband subtraction). Rather than specifying peak and sideband regions, we can fit the mass distribution to some mixture of a signal (peak) PDF $f_S(m)$ and a background (flat) PDF $f_B(m)$. From such a fit, we obtain estimated number of signal (N_S) and background (N_B) events in our dataset (and possibly some shape parameters for the signal and background PDFs). We could then assign weights to each event as in Equation (2.17),

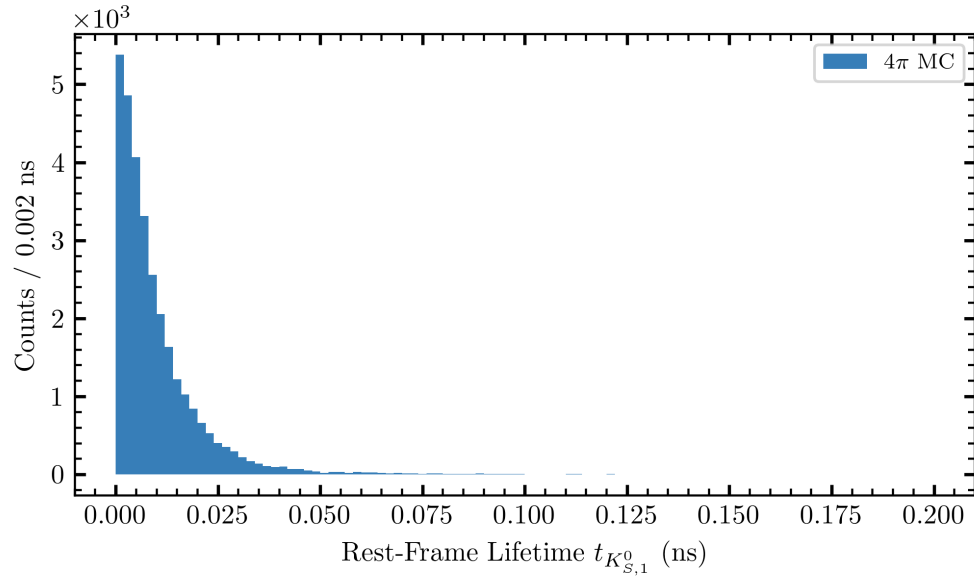$$w(m) = \frac{N_S f_S(m)}{N_S f_S(m) + N_B f_B(m)} \tag{2.17}$$

---

[10]This is stylized as $_sPlot$ in the original paper, but I find this tedious to type and to read.
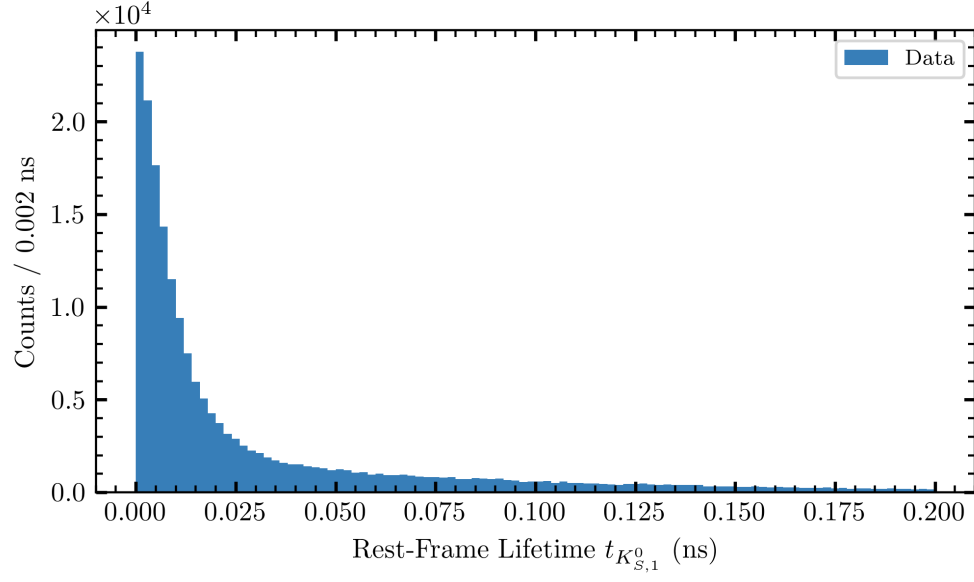
(a)
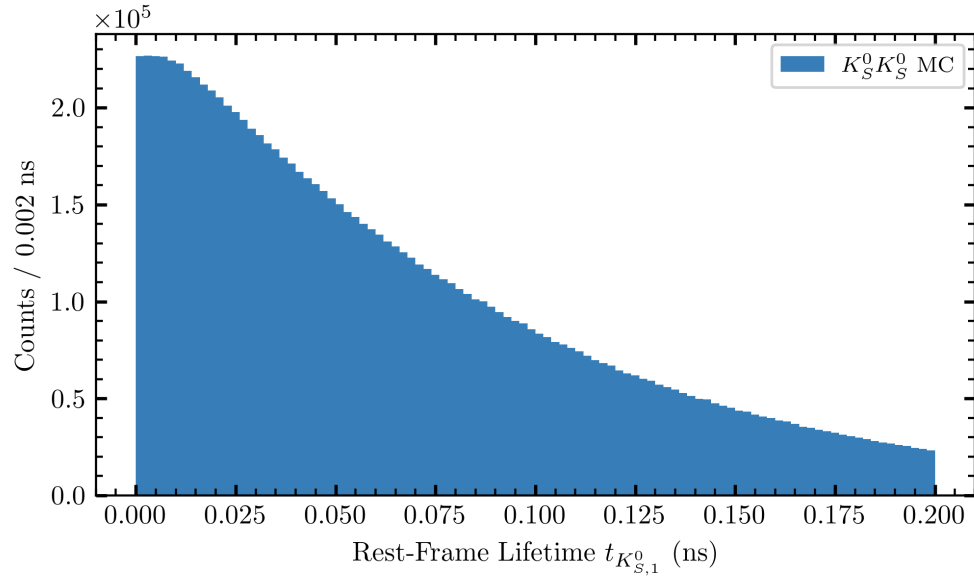
(b)

We might want to look at the "signal" inPlots for the decay angles θ and φ (control variables) in the helicity system after calculating the inPlot weights from a fit to the mass distribution (discriminating variable). However, as shown by Pivk and Le Diberder [55], we can only use inPlot in cases where the control variables are statistically dependent on the discriminating variable[11] y. In other words, our example would only be valid if $\theta = \theta(m)$ and $\phi = \phi(m)$. For the time being, let us assume that this is not the case, and that we wish to use the distribution of some variable which is statistically independent from the variables we are plotting and analyzing[12]. A correction term can be applied to give us the sPlot version of Equation (2.17),

$$w(y) = \tilde{w}(y)\frac{V_{SS}f_S(y) + V_{SB}f_B(y)}{N_S f_S(y) + N_B f_B(y)}, \quad \text{where } V_{ij}^{-1} = \sum_y \frac{\tilde{w}(y)f_i(y)f_j(y)}{(N_S f_S(y) + N_B f_B(y))^2} \tag{2.18}$$

where y represents any set of discriminating variables (not necessarily a mass), and $\tilde{w}(y)$ is any pre-existing weight associated with the event (weights from accidental subtraction, for instance). The V^{-1} matrix can also be understood as the covariance matrix between the free parameters N_S and N_B in the fit of the signal-background mixture, $V_{ij}^{-1} = -N\frac{\partial^2 \ln \mathcal{L}}{\partial N_i \partial N_j}$, although there is reason to believe that direct calculation by inverting the Hessian matrix from the fit will lead to less accurate results than the manual calculation method given in Equation (2.18) [56]. t Now that we have a method of assigning weights, we must pick the discriminating variables. As mentioned, these weighting methods work well on the classic "bump-on-a-background" distributions because it is easy to identify the signal and background PDFs, but because the mass of the kaons is constrained in the kinematic fit, the fitted mass of each kaon is just a δ-function and combination of measured masses for each $\pi^+\pi^-$ pair will yield a Normal distribution with little to no apparent background (by construction), so we must be a bit more clever in selecting discriminating variables. By examining the $\mathtt{bggen}$ analysis done in Section 2.2, we can see that most likely sources of background arise when the intermediate kaons are absent from the reaction: $\gamma p \to 4\pi p$. This reaction has the $K_S K_S$ final state, so pairs of pions which reconstruct close enough to kaons will be almost indistinguishable in the data. However, they differ in one key way, namely that the K_S intermediate contains a strange quark while the $\pi^+\pi^-$ decay state does not, so such a decay must occur via the weak interaction, which is notably slower than the strong interaction which would produce pion pairs with no intermediate kaon. In other words, while the signal's rest-frame lifetime distribution should have an exponential slope near the K_S lifetime, the background would theoretically have nearly zero rest-frame lifetime for every event, or a much smaller exponential slope in practice[13].

Therefore, we will begin by generating both a signal and background dataset in Monte Carlo. We then interpret both datasets as if they were our desired channel by running them through the GlueX reconstruction and reaction

---

[11]In practice, more than one discriminating variable can be used.

[12]Total statistical (in)dependence is a very strict requirement, but we will later see that small modifications to the sPlot method can permit amounts of dependence between the two extremes.

[13]An exponential distribution is just what best fits the rest-frame lifetime distribution in the 4π Monte Carlo and has no physical implication.

filter, as well as all of our selections up to this point. We can then fit the rest-frame lifetime of each dataset to an exponential model,

$$f(t; \lambda) = \lambda \exp\{-\lambda t\}, \tag{2.19}$$

where $\lambda \equiv 1/\tau$, the lifetime of the kaon in question. Since we have two independently decaying kaons, we should really form a joint distribution for both, where we will assume each kaon has the same average lifetime:

$$f(t_1, t_2; \lambda) = \lambda^2 \exp\{-\lambda t_1\} \exp\{-\lambda t_2\} \tag{2.20}$$

Both the signal and background distributions can be modeled in this way, giving us only two free parameters, λ_S and λ_B for the signal and background respectively, to fit.

We can then use a mixture of exponential distributions with both signal and background slopes to fit the entire dataset:

$$g(t_1, t_2; z, \lambda_S, \lambda_B) \equiv z f(t_1, t_2; \lambda_S) + (1 - z) f(t_1, t_2; \lambda_B) \tag{2.21}$$

where z is the signal fraction of the total number of events N. From its fit value, we can determine values of $N_S = z \cdot N$ and $N_B = (1 - z) \cdot N$ to use in Equation (2.18) and complete the weighting procedure. We can perform this fit by minimizing the negative log-likelihood function,

$$-2 \ln \mathcal{L}(z, \lambda_S, \lambda_B) = -2 \sum_i^N \tilde{w}_i \ln g(t_{1,i}, t_{2,i}; z, \lambda_S, \lambda_B) \tag{2.22}$$

where again, we include any pre-existing weights $\tilde{w}$ in the fit.

Examining Figure 2.13b, we can see that the expected distribution from signal Monte Carlo is not quite exponential, while the expected contribution from background Monte Carlo in Figure 2.13c is, at least in the important region of low rest-frame lifetimes. Rather than model the signal distribution analytically, we will instead use the distribution from the Monte Carlo itself as the model by binning the simulated data (a bin width of 1 ps seems to give a distribution that is decently smooth in practice). In the following discussions, we will use this binned distribution as the model for the signal component and the exponential distribution in Equation (2.20) for the background component. Because of this, the signal distribution does not have a slope parameter λ_S, so the true mixture equation looks like,

$$g(t_1, t_2; z, \lambda_B) \equiv z \tilde{f}(t_1, t_2) + (1 - z) f(t_1, t_2; \lambda_B) \tag{2.23}$$

where $\tilde{f}$ represents the binned distribution, and the equation for the likelihood is,

$$-2 \ln \mathcal{L}(z, \lambda_B) = -2 \sum_i^N \tilde{w}_i \ln g(t_{1,i}, t_{2,i}; z, \lambda_B) \tag{2.24}$$

Non-Factorizing sPlot

Over the course of the previous discussion, it was assumed that the discriminating variables, t_1 and t_2, were statistically independent from the control variables we wish to use in later analyses. The set of control variables must include all variables we use as inputs to the partial-wave analysis in Chapter 3, including the invariant mass m of the $K_S^0 K_S^0$ system and the helicity angles θ and φ of the decay. We should now confirm that the rest-frame lifetimes are statistically independent from these control variables (in other words, show that they are statistically independent). To test for statistical independence between $t_{1,2}$ and a given control variable, we first split our dataset into M evenly-spaced quantiles in that control variable, which ensures each bin gets roughly the same number of events. Next, we calculate the likelihood of a null hypothesis which assumes the variables are statistically independent by fitting all datasets simultaneously with a shared λ_B parameter. We then calculate the likelihood of an alternative hypothesis, which assumes statistical dependence, by finding the joint likelihood of independent fits of λ_B over each quantile. The result of these fits can be formulated as a likelihood ratio,

$$\Lambda = -2 \ln \frac{\sup \mathcal{L}_{H_0}}{\sup \mathcal{L}_{H_1}} = -2 \ln \frac{\sup \prod_i^M \mathcal{L}_i(z_i, \lambda_B)}{\sup \prod_i^M \mathcal{L}_i(z_i, \lambda_{B,i})} \tag{2.25}$$

where $\mathcal{L}_{H_0}$ and $\mathcal{L}_{H_1}$ are the likelihoods of the null and alternative hypotheses respectively, the supremum indicates we are maximizing these likelihoods (in a maximum likelihood fit), the product $\prod_i^M$ iterates over each quantile of data in the given control variable, and $\mathcal{L}_i$ is the likelihood evaluated over data in the ith quantile. Λ is χ^2 distributed with $M-1$ degrees of freedom (the difference between $M+1$ free parameters in the null hypothesis, a signal fraction z_i for each quantile plus the exponential background slope shared across all quantiles, and $2M$ in the alternative hypothesis, a signal fraction and one exponential slope for each quantile). The factor of 2 is required because $\ln \mathcal{L}(\theta_1, ..., \theta_i) \sim -\frac{1}{2}\chi_i^2$ asymptotically with sample size, according to Wilks' theorem. We can obtain a p-value representing the likelihood of the null hypothesis being true by evaluating the p-value:

$$p = 1 - F_{\chi_{M-1}^2}(\Lambda) \tag{2.26}$$

where $F_{\chi_{M-1}^2}(\Lambda)$ is the cumulative distribution function of a χ^2 distribution with $M-1$ degrees of freedom. Following this procedure for the invariant mass of $K_S^0 K_S^0$[14], we obtain p-values of $< 2.23 \times 10^{-308}$ with two, three, or four quantiles. The calculated p-values imply that we should reject the null hypothesis and accept that the discriminating (rest-frame lifetime) and control (invariant mass of $K_S^0 K_S^0$) variables are not statistically independent. This means we cannot use a traditional sPlot to weight our data. h The results of these tests over the data consistently return p-values close to zero (below machine precision). While this may seem surprising, the results are visualized for four quantiles in Figure 2.14, and we can see that there is a strong statistcal dependence between the control

---

[14]No significant statistical dependence was found for the helicity angles.
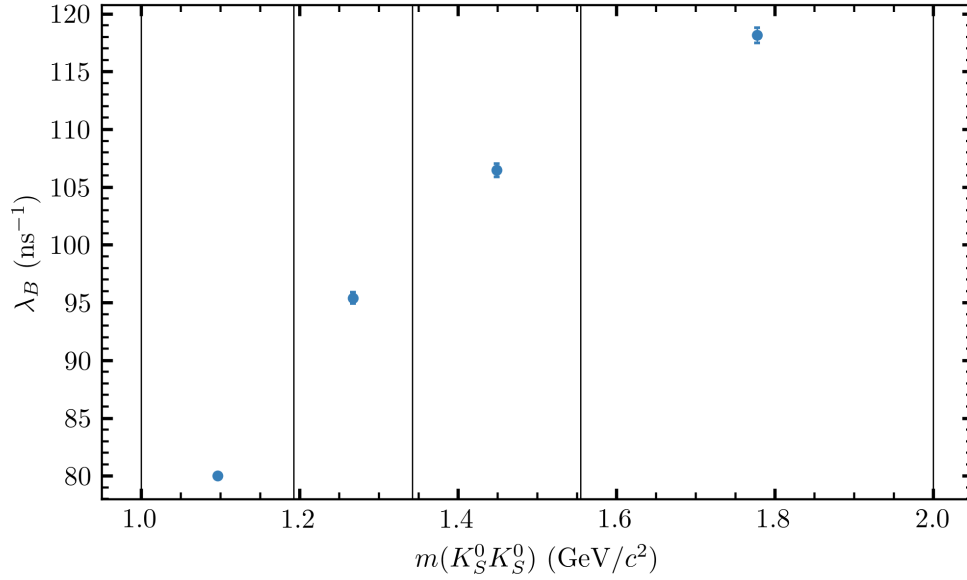
Figure 2.14: Background exponential slopes from fits over four quantiles in $m(K_S^0 K_S^0)$ (x-axis) of the rest-frame lifetime distributions of data. Both show a definite statistical dependence between rest-frame lifetime and the invariant mass of $K_S^0 K_S^0$ with a p-value smaller than machine precision ($p < 2.23 \times 10^{-308}$).

and discriminating variables which lead to this low p-value. Again, the significantly small p-values justify the use of non-factorizing sPlot across the background component, meaning that we need at least two background components in the final sPlot weighting[15].

The process for obtaining the correct weights is straightforward, we simply allow for more than one signal and background component in the fit and sum over all signal components when we calculate the final weight values [56]. Since the weights corresponding to each signal component in the sPlot can be added to each other to obtain a joint weight [55], Equation (2.18) can be extended to allow multiple signal and background components:

$$w(x) = \frac{\sum_j V_{Sj} f_j(x)}{\sum_k N_k f_k(x)}, \quad \text{where } V_{ij}^{-1} = \sum_x \frac{f_i(x) f_j(x)}{\left(\sum_k N_k f_k(x)\right)^2} \tag{2.27}$$

and S is the index of the signal component.

Application of Weights

The only thing left to do is determine how many background components we should use in the weighting procedure. To this end, we now turn to the Monte Carlo simulations of the 4π-background. By choosing a number of quantiles in invariant mass corresponding to the number of components, we can fit single exponential distributions to each

---

[15]We found that a similar analysis an exponential signal distribution also indicates a significant amount of non-factorization, but the difference in the slopes of each component are too small to give significantly different fits to the true data. Additionally, we could choose to use the Monte Carlo distribution for the background as well, but that would assume that we have correctly modeled the entire background, while we really only modeled what we believe was the most prominent component.

Method	rAIC	rBIC
$A1$	9544.558	9515.780
$A2$	6.616	<u>0.000</u>
$A3$	<u>0.000</u>	15.545
$A4$	9.318	47.024
$B1$	9565.583	9525.725
$B2$	9240.874	9212.096
$B3$	9059.066	9041.369
$B4$	9036.816	9030.199

Table 2.4: Relative AIC and BIC values for each fitting method. The absolute minimum values in each column are underlined. Methods are labeled by whether the background slopes are free (A) or fixed (B) and by the number of background components used.

quantile in the simulated background. For instance, if we chose to use three background components, we would divide the background Monte Carlo into three, and fit each quantile to an exponential distribution to obtain a set of three λ_B values. The resulting λ_B values could then be used as a starting point for a multi-component fit to the data. Alternatively, the background slopes could be fixed to the values from the fits to simulations, and only the yields would be allowed to float in the fit to data. We will refer to the first case, where the fit parameters from Monte Carlo are free, as A, the case where they are fixed as B. To select a model, we can use the relative Akaike Information Criterion (AIC) [57] and Bayesian Information Criterion (BIC) [58]:

$$r\text{AIC} \equiv \text{AIC} - \text{AIC}_{\min} \quad \text{where AIC} \equiv 2k - 2\ln\mathcal{L} \tag{2.28}$$

$$r\text{BIC} \equiv \text{BIC} - \text{BIC}_{\min} \quad \text{where BIC} \equiv k\ln N - 2\ln\mathcal{L} \tag{2.29}$$

$$\tag{2.30}$$

where k is the number of free parameters and N is the number of events in the dataset. The optimal model will minimize these criteria. In Table 2.4, all of the relative AIC and BIC values are shown. In this table, the methods are labeled A and B as described above followed by the number of background components in the fit. Since the procedure requires us to minimize rAIC and rBIC, we can see that either method $A2$ or $A3$ should be the selected model. We can see the fit results in Figure 2.15. The fit for $A3$ contains two background components with very similar slopes, so we will prefer $A2$ for simplicity and will use it in the rest of the analysis. It is interesting to note that method B, where the component slopes were fixed to values obtained from fits over background Monte Carlo, are generally much poorer fits overall, despite having fewer degrees of freedom. This possibly reflects the fact that we only modeled one source of background in the Monte Carlo, while many sources could be present in the data.

Neutral Kaon Decay Channels
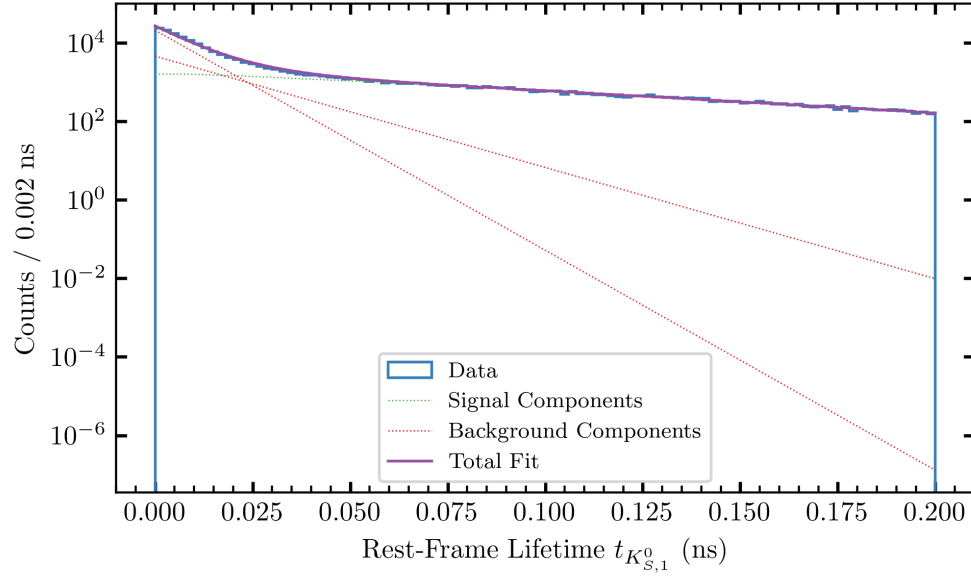
(a) The fit to data using method *A*2.
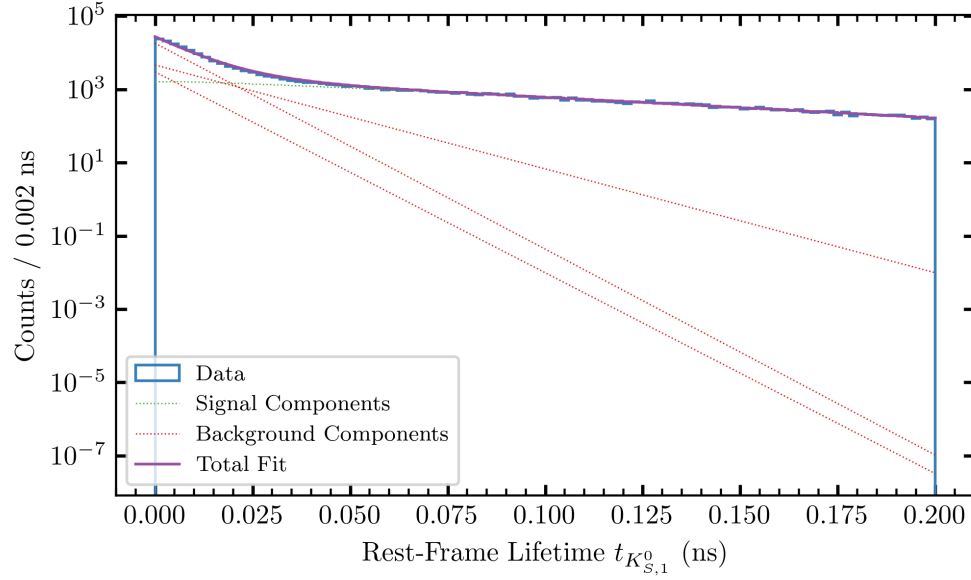
(b) The fit to data using method *A*3.

Figure 2.15: Fits of Equation (2.23) to data using method (a) *A*2 and (b) *A*3. The *A*2 configuration gives a better value for BIC, while *A*3 has a better AIC. We will use *A*2, since two of the background components of *A*3 are very similar and complicate the model unnecessarily.

Chapter 3

Partial-Wave Analysis

3.1 Amplitude Formalism

Now we embark on the topic of amplitudes. We wish to describe the dynamics of our reaction in a way that allows us to extract quantum numbers like spin from our data. There are several difficulties in doing so: First, we are trying to determine the properties of many particles at once, and we know that many resonances in this channel overlap in mass space. This precludes the use of a simple Breit-Wigner description of most of these resonances, as overlapping Breit-Wigners do not preserve unitarity. Second, the GlueX experiment uses a linearly polarized photon beam, so it behooves us to use a formalism which can include this polarization. Finally, there are many resonances in this channel, and while we have the largest photoproduction dataset to date, we are still relatively data limited, which further complicates any dynamical description. The majority of this section is a summary of the formalisms described in [59] and [60].

Single-Particle Helicity States

We begin by defining a set of observables which are independent of frames and rotations on those frames. This is known as the helicity formalism, where helicity resembles the spin projection along the axis of a particle's motion. First, we define a rotation $R(\alpha, \omega, \gamma)$ as a matrix whose action on a vector is a rotation about the Euler angles α, ω, and γ. For each rotation, we can define a unitary operator $U[R]$ which has the group property $U[R_2 R_1] = U[R_2]U[R_1]$ as it is an operator on the group $SO(3)$. Being an operator on $SO(3)$, we can also write it as

$$U[R(\alpha, \omega, \gamma)] = e^{-\imath \alpha J_z} e^{-\imath \omega J_y} e^{-\imath \gamma J_z} \tag{3.1}$$

We can then describe the matrix elements of this operator in the angular momentum eigenbasis $|jm\rangle$ (representing a spin-j particle where m is the projection of spin onto the $\hat{z}$-axis) with the Wigner D-matrix:

$$U[R(\alpha, \omega, \gamma)] \equiv \sum_{m'} |jm\rangle D^j_{m'm}(R(\alpha, \omega, \gamma)) \tag{3.2}$$

where

$$D^j_{m'm}(\alpha, \omega, \gamma) \equiv e^{-\imath m' \alpha} d^j_{m'm} e^{-\imath m \gamma} \tag{3.3}$$

and

$$d^j_{m'm}(\omega) = \left\langle jm' \middle| e^{-\imath \omega J_y} \middle| jm \right\rangle \tag{3.4}$$

We can further extend this eigenbasis to include linear momentum by introducing Lorentz boosts $L(\vec{\beta})$. We denote the operation of a boost along the $\hat{z}$-axis with velocity β as $L_z(\beta)$. A boost in any direction described by polar angles (θ, φ) can be achieved by rotating the $\hat{z}$-axis to align with the direction vector, boosting in the new $\hat{z}$-direction, and rotating back:

$$L(\vec{\beta}) = R(\varphi, \theta, 0) L_z(\beta) R^{-1}(\varphi, \theta, 0) \tag{3.5}$$

Together, the space of rotations and boosts defines the Lorentz group, where each arbitrary Lorentz transformation Λ has a unitary operator $U[\Lambda]$ with the group property $U[\Lambda_2 \Lambda_1] = U[\Lambda_2] U[\Lambda_1]$, so in terms of operators, we can also write

$$U[L(\vec{p})] = U[R(\varphi, \theta, 0)] U[L_z(p)] U^{-1}[R(\varphi, \theta, 0)] \tag{3.6}$$

Finally, this allows us to define the "canonical" basis for a single particle as

$$U[L(\vec{p})] |jm\rangle \equiv |\vec{p}, jm\rangle \tag{3.7}$$

Unfortunately, the quantum number m is only valid in the rest frame of the state because the $\hat{z}$-axis of the rest frame is not equivalent to the $\hat{z}$-axis in any arbitrarily Lorentz-transformed frame. Therefore, we will define helicity λ as the projection of spin along the direction of motion and introduce new helicity states,

$$|\vec{p}, j\lambda\rangle = U[L(\vec{p})] U[R(\varphi, \theta, 0)] |j\lambda\rangle = U[R(\varphi, \theta, 0)] U[L_z(p)] |j\lambda\rangle \tag{3.8}$$

In this definition, we have two ways of obtaining the helicity frame: We can either rotate the state first such that the quantization axis is aligned with $\vec{p}$ and then boost in the $\hat{p}$-direction or we can first boost in the $\hat{z}$-direction and then rotate. In either equivalent case, λ is invariant under rotations as well as boosts parallel to $\vec{p}$. Finally, we can define these helicity states over a basis of canonical states:

$$\left|\vec{p}, j\lambda\right\rangle = \sum_{m} D^{j}_{m\lambda}(R(\varphi, \theta, 0)) \left|\vec{p}, jm\right\rangle \tag{3.9}$$

The single-particle states are normalized such that

$$\left\langle \vec{p}', j'\lambda' \middle| \vec{p}, j\lambda \right\rangle = \tilde{\delta}(\vec{p}' - \vec{p})\delta_{j'j}\delta_{\lambda'\lambda} \tag{3.10}$$

$$\text{with } \tilde{\delta}(\vec{p}' - \vec{p}) = (2\pi)^3(2E)\delta^{(3)}(\vec{p}' - \vec{p})$$

since the Lorentz-invariant phase space element is given by $\tilde{\mathrm{d}}p = \frac{\mathrm{d}^3\vec{p}}{(2\pi)^3(2E)}$. This gives the following representation of the identity:

$$\sum_{j\lambda} \int \left|\vec{p}, j\lambda\right\rangle \tilde{\mathrm{d}}p \left\langle \vec{p}, j\lambda\right| = I \tag{3.11}$$

Two-Particle Helicity States

Of course, we would like to extend these states to be able to talk about interactions and decays. For notation, I will use Ω to represent the polar angles θ and φ and $\varnothing$ to describe the specific value of 0 for both of these angles. Similarly, R_Ω and $R_\varnothing$ will represent the corresponding rotation operators (the second being a null rotation the direction of the $\hat{z}$-axis). R without subscript or angles will represent an arbitrary rotation whose angles are not important for the derivation.

Next, we can define a joint state of two particles with masses w_1 and w_2 (to avoid confusion with angular moments) and spins s_1 and s_2. In the center-of-momentum (COM) frame, these particles are back-to-back, and we can define the momentum of particle 1 as $\vec{p}$ with direction Ω and particle 2 as $-\vec{p}$. Then the joint canonical state, up to a normalization constant $\mathcal{N}$, is given by

$$\left|\Omega, s_1m_1s_2m_2\right\rangle = \mathcal{N} U[L(\vec{p})] \left|s_1m_1\right\rangle U[L(-\vec{p})] \left|s_2m_2\right\rangle \tag{3.12}$$

Such a state can also be described with a total spin s and moment m_s:

$$\left|\Omega, sm_s\right\rangle = \sum_{m_1m_2} (s_1m_1s_2m_2 \mid sm_s) \left|\Omega, s_1m_1s_2m_2\right\rangle \tag{3.13}$$

Here, $(s_1m_1s_2m_2 \mid sm_s)$ is the Clebsch-Gordan coefficient describing the angular momentum coupling. Next, we can add additional angular momentum apart from the spin. For a system with angular momentum ℓ with moment m, we use the fact that $\langle\Omega|\ell m\rangle = Y^m_\ell(\Omega)$ (spherical harmonics) to define

$$\left|\ell m sm_s\right\rangle = \int \mathrm{d}\Omega \, Y^m_\ell(\Omega) \left|\Omega; sm_s\right\rangle \tag{3.14}$$

Next, the spin s and angular momentum ℓ can be coupled into the total angular momentum J with moment M:

$$|JM\ell m s m_s\rangle = \sum_{m\, m_s} (\ell m s m_s \mid JM) |\ell m s m_s\rangle \tag{3.15}$$

This coupled state is still in the canonical formalism, and we would like to use the helicity basis. Using Equation (3.8),

$$|\Omega, s_1\lambda_1 s_2\lambda_2\rangle = \mathcal{N}\,U[R_\Omega]\underbrace{\left(U[L_z(p)]\,|s_1\lambda_1\rangle\,U[L_{-z}(p)]\,|s_2, -\lambda_2\rangle\right)}_{|\varnothing,\,s_1\lambda_1 s_2\lambda_2\rangle} \tag{3.16}$$

To obtain states with a total angular momentum, we can integrate over the space of all rotations, weighted by Wigner D-matrices:

$$|JM s_1\lambda_1 s_2\lambda_2\rangle = \frac{N_J}{2\pi}\int \mathrm{d}R\, D_{M\mu}^{J*}(R)U[R]\,|\varnothing, s_1\lambda_1 s_2\lambda_2\rangle \tag{3.17}$$

This is, of course, incomplete, as we have not defined the normalization factor N_J or the coupling μ which relates helicities to total angular momentum. To do both, let us specify the rotation R as follows,

$$
\begin{aligned}
|JM s_1\lambda_1 s_2\lambda_2\rangle &= \frac{N_J}{2\pi}\int \mathrm{d}R\, D_{M\mu}^{J*}(R)U[R(\varphi, \theta, \gamma)]\,|\varnothing, s_1\lambda_1 s_2\lambda_2\rangle \\
&= \frac{N_J}{2\pi}\int \mathrm{d}R\, D_{M\mu}^{J*}(R)U[R(\varphi, \theta, 0)]U[R(0, 0, \gamma)]\,|\varnothing, s_1\lambda_1 s_2\lambda_2\rangle \\
&= \frac{N_J}{2\pi}\int \mathrm{d}R\, D_{M\mu}^{J*}(R)e^{-\imath(\lambda_1-\lambda_2)\gamma}U[R(\varphi, \theta, 0)]\,|\varnothing, s_1\lambda_1 s_2\lambda_2\rangle \\
&= \frac{N_J}{2\pi}\int \mathrm{d}\Omega\,\mathrm{d}\gamma\, e^{\imath M\varphi} d_{M\mu}^{J*}e^{\imath\mu\gamma} e^{-\imath(\lambda_1-\lambda_2)\gamma}U[R(\varphi, \theta, 0)]\,|\varnothing, s_1\lambda_1 s_2\lambda_2\rangle \\
&= \frac{N_J}{2\pi}\int \mathrm{d}\Omega\,\mathrm{d}\gamma\, e^{\imath M\varphi} d_{M\mu}^{J*}e^{\imath(\mu-(\lambda_1-\lambda_2))\gamma}\,|\Omega, s_1\lambda_1 s_2\lambda_2\rangle \\
&= N_J\int \mathrm{d}\Omega\, D_{M\lambda}^{J*}(R_\Omega)\,|\Omega, s_1\lambda_1 s_2\lambda_2\rangle
\end{aligned}
\tag{3.18}
$$

with $\lambda = \lambda_1 - \lambda_2$

It can be shown that the normalization is $\mathcal{N} = \frac{1}{4\pi}\sqrt{\frac{p}{\sqrt{s}}}$ where p is the relative momentum and $\sqrt{s}$ the center-of-momentum energy the two-particle system (s is the Mandelstam variable). The normalization of the standard two-particle states is given by

$$\left\langle \Omega', s_1'\lambda_1' s_2'\lambda_2' \middle| \Omega, s_1\lambda_1 s_2\lambda_2 \right\rangle = \delta^{(2)}(\Omega' - \Omega)\delta_{s_1' s_1}\delta_{\lambda_1'\lambda_1}\delta_{s_2' s_2}\delta_{\lambda_2'\lambda_2} \tag{3.19}$$

This follows immediately from Section 3.1. Next, to ensure that

$$\left\langle J'M' s_1'\lambda_1' s_2'\lambda_2' \middle| JM s_1\lambda_1 s_2\lambda_2 \right\rangle = \delta_{J'J}\delta M'M\delta_{s_1' s_1}\delta_{\lambda_1'\lambda_1}\delta_{s_2' s_2}\delta_{\lambda_2'\lambda_2} \tag{3.20}$$

we must have $N_J = \sqrt{\frac{2J+1}{4\pi}}$. Finally,

$$\left\langle \Omega, s_1' \lambda_1' s_2' \lambda_2' | J M s_1 \lambda_1 s_2 \lambda_2 \right\rangle = N_J D_{M\lambda}^{J*}(R_\Omega) \delta_{s_1' s_1} \delta_{\lambda_1' \lambda_1} \delta_{s_2' s_2} \delta_{\lambda_2' \lambda_2} \tag{3.21}$$

Production Amplitudes

Given the two-particle helicity states, we can now construct production amplitudes which will model what we measure in the experiment.

We approach this with the S-matrix formalism. We assert that all of the dynamics of any reaction $i \to f$ are elements of an invariant scattering matrix S written $\langle f | S | i \rangle$. We then define the matrix T such that $S = 1 + 2\iota T$, called the transition matrix[1].

Let us examine the reaction $a + b \to c + d$. We can write the invariant S-matrix element as

$$\left\langle \vec{p}_c \lambda_c; \vec{p}_d \lambda_d | S | \vec{p}_a \lambda_a; \vec{p}_b \lambda_b \right\rangle = (4\pi)^2 \sqrt{\frac{s}{p_f p_i}} \left\langle \Omega \lambda_c \lambda_d | S(\sqrt{s}) | \varnothing \lambda_a \lambda_b \right\rangle \tag{3.22}$$

where we have used Equation (3.16) to write the states with an initial momentum $(-)\vec{p}_i$ for particle $(b)a$ pointing along the direction $(\theta, \varphi) = (0, 0) \equiv \varnothing$ and a final momentum $(-)\vec{p}_f$ for particle $(d)c$ pointing in the direction Ω with respect to $\vec{p}_i$. We can replace S with the definition of T to arrive at a similar formula for the invariant transition amplitude $\mathcal{M}_{fi}$,

$$\mathcal{M}_{fi} = (4\pi)^2 \sqrt{\frac{s}{p_f p_i}} \left\langle \Omega \lambda_c \lambda_d | T(\sqrt{s}) | \varnothing \lambda_a \lambda_b \right\rangle \tag{3.23}$$

While we will not measure a cross-section exactly, we will roughly measure the number of events as a function of mass and helicity angles, which is proportional to the cross section. We refer to this as the "intensity" function (see Appendix B of [59]),

$$I(m, \Omega) \propto \frac{\partial^2 \sigma}{\partial m \partial \Omega} \equiv \frac{p_f}{p_i} \left| \frac{\mathcal{M}_{fi}}{8\pi \sqrt{s}} \right|^2 \tag{3.24}$$

We can also use this formalism to model two-body decays of the form $c \to 1 + 2$, where c has total angular momentum J. Starting in the rest frame of particle c, we say that particle $(2)1$ has momentum $(-)\vec{p}$, so the amplitude for a particular angular moment M can be written as

---

[1] The factor of 2ι here is purely convention and makes some derivations more compact.

$$\left\langle \vec{p}\lambda_1; -\vec{p}\lambda_2 \middle| \mathcal{M} \middle| JM \right\rangle = \left\langle \vec{p}\lambda_1; -\vec{p}\lambda_2 \middle| JM\lambda_1\lambda_2 \right\rangle \left\langle JM\lambda_1\lambda_2 \middle| \mathcal{M} \middle| JM \right\rangle \tag{3.25}$$

$$= 4\pi \sqrt{\frac{w}{p}} \underbrace{\left\langle \Omega\lambda_1; -\vec{p}\lambda_2 \middle| JM\lambda_1\lambda_2 \right\rangle}_{N_J D^{J*}_{M\lambda}(\Omega)} \left\langle JM\lambda_1\lambda_2 \middle| \mathcal{M} \middle| JM \right\rangle \tag{3.26}$$

$$\equiv N_J D^{J*}_{M\lambda}(\Omega) F^J_{\lambda_1\lambda_2} \tag{3.27}$$

where w is the effective mass of the decaying particle, $\lambda = \lambda_1 - \lambda_2$, and we use the completeness relation $\sum_{JM\lambda_1\lambda_2} |JM\lambda_1\lambda_2\rangle \langle JM\lambda_1\lambda_2| = 1$ along with Equation (3.21). We call $F^J_{\lambda_1\lambda_2}$ the helicity decay amplitude.

If we wish to model $X \to K^0_S K^0_S$, we first recognize that the kaon is a spin-0 particle, so the difference in helicity is $\lambda = 0$. Therefore,

$$I(m, \Omega) \propto |\mathcal{M}_{fi}|^2 \sim \left| N_J D^{J*}_{M0}(\Omega) F^J(m) \right|^1 = \left| Y^M_J(\Omega) F^J(m) \right|^2 \tag{3.28}$$

Since we cannot know the spin projection of a particle *a priori*, we will typically obtain it from fitting the intensity to a sum over these spherical harmonics, assigning a coefficient a^J_M to each and determining the spin from the best-fitting harmonic,

$$I(m, \Omega) \propto \left| \sum_{JM} a^J_M F^J(m) Y^M_J(\Omega) \right|^2 \tag{3.29}$$

It is important to remember here that Ω has always been defined in terms of the helicity angles of the decay, i.e. the spherical angles with respect to the direction of particle X's motion found after boosting to the helicity frame. This frame is defined as the rest-frame of X (found by boosting first from the lab frame to the center-of-momentum) with $\hat{z}$ defined as the boost direction from the center-of-momentum frame, $\hat{y}$ as normal to the production plane (the plane in which the beam and recoil proton move), and $\hat{x} = \hat{y} \times \hat{z}$.

Including Linear Photon Polarization

As the GlueX beam has a known polarization, we can take advantage of this extra information to explore the parity exchanged in our reaction. Mathieu et al. [61] provide a derivation which begins with a slightly different representation of the scattering matrix, written in terms of spin-density matrix elements $\rho^\gamma_{\lambda\lambda'}$ describing the coupling of a polarized photon to the helicity of the proton target (and that of the recoiling proton product):

$$I(m, \Omega) \propto \frac{p_f}{p_i} \left| \frac{\mathcal{M}_{fi}}{8\pi\sqrt{s}} \right|^2 = \kappa \sum_{\lambda\lambda'\lambda_p\lambda_{p'}} A_{\lambda;\lambda_p\lambda_{p'}}(m, \Omega) \rho^\gamma_{\lambda\lambda'} A^*_{\lambda';\lambda_1\lambda_2}(m, \Omega) \tag{3.30}$$

where

$$\kappa(m, s) = \frac{1}{(2\pi)^3} \frac{1}{4\pi} \frac{1}{2\pi} \frac{1}{2} \frac{\sqrt{\lambda\left(m^2, m^2_{K^0_S}, m^2_{K^0_S}\right)}}{16m(s - m^2_p)^2} \tag{3.31}$$

where $\lambda(a, b, c) \equiv a^2 + b^2 + c^2 - 2(ab + bc + ca)^2$ and we define the reaction as $\gamma p \rightarrow X p'$ with $X \rightarrow K^0_S K^0_S$. Here, the indices λ and λ' couple the helicity of the incident photon to the amplitude A, while λ_p and $\lambda_{p'}$ correspond to the helicity of the target and recoiling proton, respectively. Note that these nucleon helicities are not measured at GlueX, but we will keep them in our model for the sake of completeness. Additionally, since the Mandelstam variable s only shows up in this term, we will suppress its notation for now, but will bring it back at the end of the derivation.

The spin-density matrix for the photon, $\rho^\gamma_{\lambda\lambda'}$, can be written in terms of the polarization vector,

$$\rho^\gamma_{\lambda\lambda'} = \frac{1}{2}\left(I + \vec{P}_\gamma \cdot \vec{\sigma}\right) \tag{3.32}$$

where $\vec{\sigma}$ are the Pauli matrices and

$$\vec{P}_\gamma = P_\gamma \begin{bmatrix} -\cos(2\Phi) \\ -\sin(2\Phi) \\ 0 \end{bmatrix} \tag{3.33}$$

for linearly polarized photons with polarization degree $P_\gamma \in [0, 1]$ and polarization angle Φ (measured with respect to the production plane). From here, we can expand the intensity into three terms,

$$I(m, \Omega, P_\gamma, \Phi) = I^0(m, \Omega) - P_\gamma I^1(m, \Omega) \cos(2\Phi) - P_\gamma(m, \Omega) \sin(2\Phi) \tag{3.34}$$

where

$$I^0(m, \Omega) = \frac{\kappa}{2} \sum_{\lambda\lambda_p\lambda_{p'}} A_{\lambda;\lambda_p\lambda_{p'}}(m, \Omega) A^*_{\lambda;\lambda_p\lambda_{p'}}(m, \Omega) \tag{3.35}$$

$$I^1(m, \Omega) = \frac{\kappa}{2} \sum_{-\lambda\lambda_p\lambda_{p'}} A_{\lambda;\lambda_p\lambda_{p'}}(m, \Omega) A^*_{\lambda;\lambda_p\lambda_{p'}}(m, \Omega) \tag{3.36}$$

$$I^2(m, \Omega) = \imath\frac{\kappa}{2} \sum_{\lambda\lambda_p\lambda_{p'}} \lambda A_{-\lambda;\lambda_p\lambda_{p'}}(m, \Omega) A^*_{\lambda;\lambda_p\lambda_{p'}}(m, \Omega) \tag{3.37}$$

Next, we can write

$$A_{\lambda;\lambda_p\lambda_{p'}} = a^J_{M;\lambda\lambda_p\lambda_{p'}} F^J_{\lambda\lambda_p\lambda_{p'}}(m) Y^M_J(\Omega) \tag{3.38}$$

---

[2]It is unfortunate that the notation for this function is typically written with a λ, and we will attempt to ensure the distinction from helicity is clear when we use it.

For clarity, we will absorb the coefficient a into the mass-dependent term F and define

$$T^J_{M;\lambda\lambda_p\lambda_{p'}}(m) \equiv a_{JM;\lambda\lambda_p\lambda_{p'}} F^J_{\lambda\lambda_p\lambda_{p'}}(m) \tag{3.39}$$

As mentioned, the polarization of the beam gives us access to information about the parity of the exchanged particle in the t-channel reaction. For this, we work in the "reflectivity" basis,

$$T^{J(\epsilon)}_{M;\lambda_p\lambda_{p'}}(m) \equiv \frac{1}{2}\left[T^J_{M;+,\lambda_p\lambda_{p'}}(m) - \epsilon(-1)^M T^J_{-M;-,\lambda_p\lambda_{p'}}(m) \right] \tag{3.40}$$

This basis is useful, as it can be shown that in the high-energy limit, the reflectivity $\epsilon = \pm 1$ corresponds to the exchanged naturality in t-channel reactions[3]. Furthermore, parity invariance leads to the relation

$$T^{J(\epsilon)}_{M;-\lambda_p-\lambda_{p'}}(m) = \epsilon(-1)^{\lambda_p - \lambda_{p'}} T^{J(\epsilon)}_{M;\lambda_p\lambda_{p'}}(m) \tag{3.41}$$

so there are really only two unique partial waves, those where the proton helicity flips ($\eta = -1$) and those where it does not ($\eta = +1$), which we will write as $T^{J(\epsilon)}_{M;\eta}$:

$$T^{J(\epsilon)}_{M;+}(m) \equiv T^{J(\epsilon)}_{M;++}(m) \qquad T^{J(\epsilon)}_{M;-}(m) \equiv T^{J(\epsilon)}_{M;+-}(m) \tag{3.42}$$

3.2   The Z^m_ℓ Amplitude

The next part of the derivation pertains to both how we formulate this amplitude in practice and how we define sets of waves with which to fit our data, and it closely follows the work of Shepherd GlueXdoc4094.

We can rewrite the intensity function in Equation (3.34) in terms of exponentials. We will also expand out the sums over $\lambda = \pm$, the photon helicity, and temporarily suppress the indices of nucleon helicity for clarity (although I will keep the sum to remind us that these indices exist on each A).

$$I(m, \Omega, P_\gamma, \Phi) = \frac{\kappa}{2} \sum_{\lambda_p\lambda_{p'}} \left[A_-(m,\Omega)A^*_-(m,\Omega) + A_+(m,\Omega)A^*_+(m,\Omega) \right.$$

$$\left. - P_\gamma e^{i2\Phi} A_-(m,\Omega)A^*_+(m,\Omega) - P_\gamma e^{-i2\Phi} A_+(m,\Omega)A^*_-(m,\Omega) \right] \tag{3.43}$$

Next, we define polarized amplitudes,

$$f\tilde{A}_\pm(m,\Omega,\Phi) \equiv e^{\mp i\Phi} A_\pm(m,\Omega), \tag{3.44}$$

---

[3]i.e. Positive reflectivity implies natural parity exchange and negative reflectivity implies unnatural parity exchange

e so that the intensity can be written as l

$$\frac{\kappa}{4} \sum_{\lambda_p \lambda_{p'}} \left[(1 - P_\gamma) \left| \tilde{A}_+(m, \Omega, \Phi) + \tilde{A}_-(m, \Omega, \Phi) \right|^2 + (1 + P_\gamma) \left| \tilde{A}_+(m, \Omega, \Phi) - \tilde{A}_-(m, \Omega, \Phi) \right|^2 \right] \tag{3.45}$$

Rewriting these polarized amplitudes in terms of those of Equation (3.40), we find

$$\tilde{A}_+(m, \Omega, \Phi) = \sum_{\lambda_p \lambda_{p'}} \sum_{J,M} \left[T_M^{J(-)}(m) + T_M^{J(+)}(m) \right] e^{-\iota\Phi} Y_J^M(\Omega) \tag{3.46}$$

$$\tilde{A}_-(m, \Omega, \Phi) = \sum_{\lambda_p \lambda_{p'}} \sum_{J,M} \left[T_M^{J(-)}(m) - T_M^{J(+)}(m) \right] e^{-\iota\Phi} Y_J^{M*}(\Omega) \tag{3.47}$$

$$\tag{3.48}$$

We now define the function,

$$\hat{Z}_J^M(\Omega, \Phi) \equiv e^{-\iota\Phi} Y_J^M(\Omega) \tag{3.49}$$

This allows us to rewrite Equation (3.45) as

$$I(m, \Omega, P_\gamma, \Phi) = \sum_{\lambda_p \lambda_{p'}} \kappa \left\{ (1 - P_\gamma) \left| T_M^{J(-)}(m) \operatorname{Re}[\hat{Z}_J^M(\Omega, \Phi)] + \iota T_M^{J(+)}(m) \operatorname{Im}[\hat{Z}_J^M(\Omega, \Phi)] \right|^2 \right. \tag{3.50}$$

$$\left. + (1 + P_\gamma) \left| T_M^{J(+)}(m) \operatorname{Re}[\hat{Z}_J^M(\Omega, \Phi)] + \iota T_M^{J(-)}(m) \operatorname{Im}[\hat{Z}_J^M(\Omega, \Phi)] \right|^2 \right\} \tag{3.51}$$

$$\tag{3.52}$$

Next, we recognize the parity invariance mentioned in Equation (3.41) to transform the intensity into four coherent sums. To demonstrate this, we will show the expansion of the first coherent sum given in Equation (3.52), suppressing m, Ω and Φ for simplicity:

$$\sum_{\lambda_p \lambda_{p'}} \left| \sum_{JM} \left(T_{M;\lambda_p\lambda_{p'}}^{J(-)} \operatorname{Re}[\hat{Z}_J^M] + \iota T_{M;\lambda_p\lambda_{p'}}^{J(+)} \operatorname{Im}[\hat{Z}_J^M] \right) \right|^2$$

$$= \sum_{\lambda_p \lambda_{p'}} \sum_{JM} \sum_{J'M'} \left(T_{M;\lambda_p\lambda_{p'}}^{J(-)} \operatorname{Re}[\hat{Z}_J^M] + \iota T_{M;\lambda_p\lambda_{p'}}^{J(+)} \operatorname{Im}[\hat{Z}_J^M] \right) \left(T_{M';\lambda_p\lambda_{p'}}^{J'(-)*} \operatorname{Re}[\hat{Z}_{J'}^{M'}] + \iota T_{M';\lambda_p\lambda_{p'}}^{J'(+)*} \operatorname{Im}[\hat{Z}_{J'}^{M'}] \right)$$

$$= \sum_{\lambda_p \lambda_{p'}} \sum_{JM} \sum_{J'M'} \left\{ \left(T_{M;\lambda_p\lambda_{p'}}^{J(-)} T_{M';\lambda_p\lambda_{p'}}^{J'(-)*} \operatorname{Re}[\hat{Z}_J^M] \operatorname{Re}[\hat{Z}_{J'}^{M'}] \right) - \left(T_{M;\lambda_p\lambda_{p'}}^{J(+)} T_{M';\lambda_p\lambda_{p'}}^{J'(+)*} \operatorname{Im}[\hat{Z}_J^M] \operatorname{Im}[\hat{Z}_{J'}^{M'}] \right) \right. \tag{3.53}$$

$$\left. + \iota \left(T_{M;\lambda_p\lambda_{p'}}^{J(-)} T_{M';\lambda_p\lambda_{p'}}^{J'(+)*} \operatorname{Re}[\hat{Z}_J^M] \operatorname{Im}[\hat{Z}_{J'}^{M'}] \right) + \iota \left(T_{M;\lambda_p\lambda_{p'}}^{J(+)} T_{M';\lambda_p\lambda_{p'}}^{J'(-)*} \operatorname{Im}[\hat{Z}_J^M] \operatorname{Re}[\hat{Z}_{J'}^{M'}] \right) \right\}$$

Next, we use the relation

$$\sum_{\lambda_p \lambda_{p'}} T_{M;\lambda_p\lambda_{p'}}^{J(\epsilon)} T_{M';\lambda_p\lambda_{p'}}^{J'(\epsilon')*} = (1 + \epsilon\epsilon') \sum_\eta T_{M;\eta}^{J(\epsilon)} T_{M';\eta}^{J'(\epsilon')*} \tag{3.54}$$

from parity conservation, which causes the last two terms in Equation (3.53) to vanish. The remaining terms can be rewritten as coherent sums, yielding the following expression for the intensity:

$$
I(m,\Omega,P_\gamma,\Phi) = 2\kappa \sum_\eta \left\{ (1-P_\gamma)\left|\sum_{JM} T_{M;\eta}^{J(-)}(m)\,\mathrm{Re}[\hat{Z}_J^M(\Omega,\Phi)]\right|^2 + (1-P_\gamma)\left|\sum_{JM} T_{M;\eta}^{J(+)}(m)\,\mathrm{Im}[\hat{Z}_J^M(\Omega,\Phi)]\right|^2 \right.
$$
$$
\left. (1+P_\gamma)\left|\sum_{JM} T_{M;\eta}^{J(+)}(m)\,\mathrm{Re}[\hat{Z}_J^M(\Omega,\Phi)]\right|^2 + (1+P_\gamma)\left|\sum_{JM} T_{M;\eta}^{J(-)}(m)\,\mathrm{Im}[\hat{Z}_J^M(\Omega,\Phi)]\right|^2 \right\} \tag{3.55}
$$

We can absorb the factors of $(1\pm P_\gamma)$ by defining the function

$$
Z_J^{M(\pm)}(\Omega,P_\gamma,\Phi) = \left(\sqrt{1\pm P_\gamma} + \imath\sqrt{1\mp P_\gamma}\right)\hat{Z}_J^M(\Omega,\Phi) \tag{3.56}
$$

We finally note that in the energy range of this reaction, we do not expect to make states with additional angular momentum L, so for our interests, J corresponds to spin. However, to be consisent with common nomenclature on this topic, we will use the notation (ℓ, m) in lieu of (J, M) and consider ℓ to correspond to spin. Previously, it was mentioned that we have no way to measure the helicity of the proton before or after this reaction, so in practice we ignore the summation over η. However, we should be cautious of the phase-space factor κ, as it depends on both m and s. This is not an issue in (mass) binned fits, which we will see later, as we average over m anyway and assume the bins are small enought that s does not vary much in each bin, but this term is non-negligable in mass-dependent formulations.

$$
I(m,s,\Omega,P_\gamma,\Phi) = 2 \sum_\eta \left\{ \left|\sum_{JM} \hat{T}_{M;\eta}^{J(-)}(m,s)\,\mathrm{Re}[Z_J^M(\Omega,P_\gamma,\Phi)]\right|^2 + \left|\sum_{JM} \hat{T}_{M;\eta}^{J(+)}(m,s)\,\mathrm{Im}[Z_J^M(\Omega,P_\gamma,\Phi)]\right|^2 \right.
$$
$$
\left. \left|\sum_{JM} \hat{T}_{M;\eta}^{J(+)}(m,s)\,\mathrm{Re}[Z_J^M(\Omega,P_\gamma,\Phi)]\right|^2 + \left|\sum_{JM} \hat{T}_{M;\eta}^{J(-)}(m,s)\,\mathrm{Im}[Z_J^M(\Omega,P_\gamma,\Phi)]\right|^2 \right\} \tag{3.57}
$$

where $\hat{T}_{M;\eta}^{J(\epsilon)}(m,s) \equiv \kappa^2(m,s)T_{M;\eta}^{J(\epsilon)}(m)$

Finally, we can choose a parameterization for $\hat{T}_{M;\eta}^{J(\epsilon)}(m,s) \to \hat{T}_{M;\eta}^{J(\epsilon)}(\vec{\beta};m,s)$. These $\vec{\beta} \in \mathbb{C}^d$ are free parameters in our models.

This gives us a generalized intensity function for linearly polarized photoproduction,

$$
\mathcal{I}(\vec{\beta};m,s,\Omega,P_\gamma,\Phi) = 2 \sum_\eta \left\{ \left|\sum_{JM} \hat{T}_{M;\eta}^{J(-)}(\vec{\beta};m,s)\,\mathrm{Re}[Z_J^M(\Omega,P_\gamma,\Phi)]\right|^2 + \left|\sum_{JM} \hat{T}_{M;\eta}^{J(+)}(\vec{\beta};m,s)\,\mathrm{Im}[Z_J^M(\Omega,P_\gamma,\Phi)]\right|^2 \right.
$$
$$
\left. \left|\sum_{JM} \hat{T}_{M;\eta}^{J(+)}(\vec{\beta};m,s)\,\mathrm{Re}[Z_J^M(\Omega,P_\gamma,\Phi)]\right|^2 + \left|\sum_{JM} \hat{T}_{M;\eta}^{J(-)}(\vec{\beta};m,s)\,\mathrm{Im}[Z_J^M(\Omega,P_\gamma,\Phi)]\right|^2 \right\} \tag{3.58}
$$

The simplest model we can parameterize is one in which we bin the data in mass m and let $T_{M;\eta}^{J(\epsilon)}(\vec{\beta};m) = \beta_i$ for the ith mass bin. This is equivalent to modeling the mass dependence as a piecewise function where each segment is

constant. We will discuss such parameterizations in Section 4.2. In the next section, we will discuss a more complex mass-dependent parameterization.

3.3 The K-Matrix Parameterization

If we wish to parameterize the amplitude $T(m)$ as a function of mass, there are several options. Perhaps the most ubiquitous is the resonant lineshape devised by Breit and Wigner in 1936 [62] whose amplitude can be written as a function of the invariant mass m,

$$T(m; M, \Gamma) = \frac{M\Gamma/\sqrt{\pi}}{(M^2 - m^2) - \imath M\Gamma} \tag{3.59}$$

where M and Γ describe the centroid and width of the peak respectively. We typically relate the centroid to the mass of the resonance and the width to the inverse of the lifetime. This is the non-relativistic form, and we can see that

$$|T(m; M, \Gamma)|^2 = \frac{(M\Gamma)^2/\pi}{(m^2 - M^2)^2 + (M\Gamma)^2} \tag{3.60}$$

which can be seen to be a Cauchy distribution.

We could continue in this way and define the mass-dependent dynamics of our system as a sum of Breit-Wigner distributions. However, this is not the correct approach, as we will show that this does not preserve the unitarity of the S-matrix. Let us examine an alternate formulation, which we will call the K-matrix method. We will see that this K-matrix yields a Breit-Wigner for a single resonance in a single decay channel, but it can be extended to multiple resonances in multiple channels while preserving unitarity.

Following the derivation by Chung et al. [63], we begin with our definition of the transition operator from Section 3.1,

$$S = I + 2\imath T \tag{3.61}$$

To conserve probability, we require the S matrix to be unitary, i.e. $SS^\dagger = S^\dagger S = I$. Plugging in the definition of T, we see that

$$I = (I + 2\imath T)(I - 2\imath T^\dagger)$$

$$I = I + 2TT^\dagger + 2\imath T - 2\imath T^\dagger$$

$$T - T^\dagger = 2\imath TT^\dagger \tag{3.62}$$

We then by the inverse of each matrix,

$$T(T^\dagger)^{-1} - I = 2\iota T$$

$$(T^\dagger)^{-1} - T^{-1} = 2\iota I$$

$$(T^{-1} + \iota I)^\dagger = T^{-1} + \iota I \tag{3.63}$$

Next, we introduce the K-matrix, defined as

$$K^{-1} = T^{-1} + \iota I \tag{3.64}$$

K is Hermitian by Equation (3.63), and by time reversal invariance of T, K must be symmetric. For simplicity, we can also choose $K \in \mathbb{R}^n$. Continuing from the previous equation,

$$I = T^{-1}K + \iota K$$

$$T = K + \iota TK \tag{3.65}$$

However, we could also reverse the order of multiplication here,

$$K^{-1}T = I + \iota T$$

$$T = K + \iota KT \tag{3.66}$$

Therefore, K and T commute. Furthermore, we can solve for T to find

$$T - \iota TK = K$$

$$T(I - \iota K) = K$$

$$T = K(I - \iota K)^{-1} \tag{3.67}$$

For a single channel, the S-matrix is scalar and can be written in the form $S = e^{2\iota\delta}$.

An Argand diagram plots the real and imaginary parts of T in the complex plane. By the definition of T along with this definition of S, unitarity-preserving trajectories for T must lie within a circle of radius $1/2$ centered at $0 + \frac{1}{2}\iota$, which we refer to as the unitary circle. Since K is defined from a unitary T- and S-matrix, it will always preserve unitarity as long as its properties of Hermiticity and symmetry are met. Therefore, any real symmetric K-matrix will yield a unitary S-matrix.

Next, we must choose how to parameterize this K-matrix and write it in a Lorentz-invariant form.
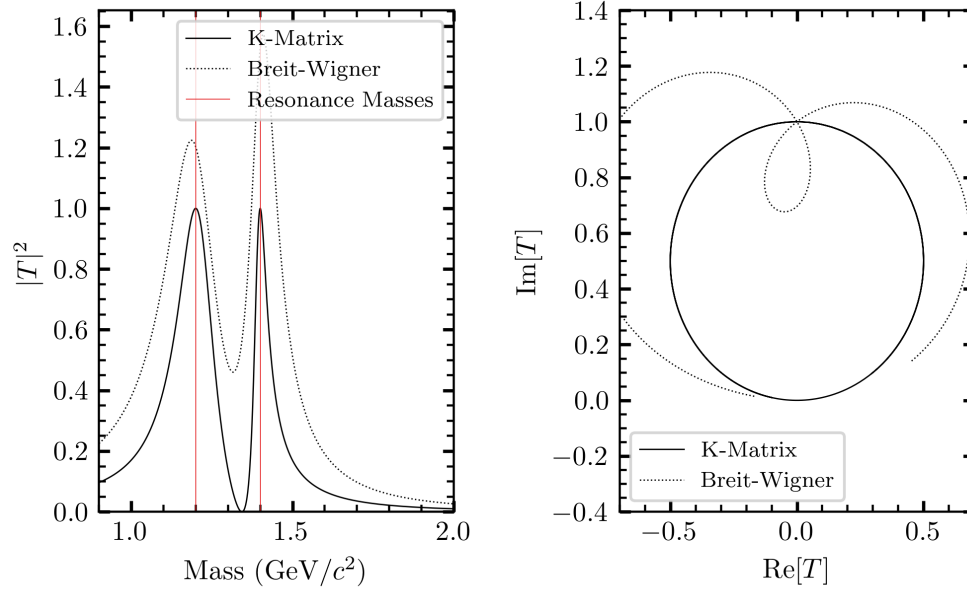
Figure 3.1: An Argand diagram depicting two fictitious resonances with masses of $1.2\,\text{GeV}/c^2$ and $1.4\,\text{GeV}/c^2$ and widths of $200\,\text{MeV}/c^2$ and $100\,\text{MeV}/c^2$ respectively using both the K-matrix formalism and interfering Breit-Wigners. The T-matrix formed from Breit-Wigners exceeds the unitary circle, implying that this construction breaks unitarity, while the K-matrix does not.

Resonances as Poles of the K-matrix

Resonances can be parametrized either as constant elements in the K-matrix, which are usually interpreted as "molecular" resonances resulting from the exchange of force-carrying bosons, or from poles, which are thought of as the resonances describing decaying hadrons [64]. While we are more interested in the second case, we will include a linear combination of poles and constant terms in the parameterization, as follows:

$$K_{ij}(m) = \sum_{\alpha} \frac{g_{\alpha i}(m)g_{\alpha j}(m)}{m_{\alpha}^2 - m^2} + c_{ij} \tag{3.68}$$

Here, α indexes the resonances, with m_{α} corresponding to the pole mass[4] of the αth resonance and $g_{\alpha i}$ corresponding to a term coupling the αth resonance to the ith decay channel. c_{ij} denotes any constant terms mentioned in the previously.

For a single resonance in a single channel, we can write the T-matrix as

$$T = K(I - \imath K)^{-1} \tag{3.69}$$

$$= \frac{\frac{g^2(m)}{m_{\alpha}^2 - m^2}}{1 - \imath \left(\frac{g^2(m)}{m_{\alpha}^2 - m^2} \right)} \tag{3.70}$$

---

[4]This is not necessarily the same value as the centroid of a Breit-Wigner fit to the same data.

$$= \frac{g^2(m)}{m_\alpha^2 - m^2 - \imath g^2(m)} \tag{3.71}$$

which we see is identical to the Breit-Wigner form given in Equation (3.59) with $g^2(m) = m_\alpha \Gamma_\alpha(m)$[5].

Furthermore, we can now demonstrate the fundamental reason why we need to use the K-matrix in lieu of Breit-Wigners when describing multiple overlapping resonances. Figure 3.1 shows that, even in a single channel, two interfering Breit-Wigners do not preserve unitarity, while the corresponding K-matrix does.

In the case where a resonance can decay into multiple channels, we say that $\Gamma_\alpha(m) = \sum_i \Gamma_{\alpha i}(m)$ is the total width and $\Gamma_{\alpha i}(m)$ are called the partial widths. In the relativistic form of the Breit-Wigner (and the Lorentz-invariant form of the resulting S-matrix), widths (and therefore partial widths) are given by

$$\Gamma_{\alpha i} = \gamma_{\alpha i}^2 \Gamma_\alpha B_{\alpha i}^\ell(m) \sqrt{\rho_i(m)} \tag{3.72}$$

where $\gamma_{\alpha i}^2$ is the fraction of the total width[6], Γ_α, which is coupled to the channel i, and $\rho_i(m)$ is the phase space factor

$$\rho_i(m) = \sqrt{\chi_i^+(m)\chi_i^-(m)} \quad \text{where} \quad \chi_i^\pm = 1 - \left(\frac{m_1 \pm m_2}{m} \right)^2 \tag{3.73}$$

when the ith channel describes the decay $\alpha \to 1 + 2$ and $B_{\alpha i}^\ell(m)$ is the centrifugal barrier factor describing the suppression to the partial width when a resonance has angular momentum ℓ. We typically parameterize this via form factors derived by Blatt and Weisskopf [65],

$$B_{\alpha i}^\ell(m) = \frac{F_\ell(z_i(m))}{F_\ell(z_i(m_\alpha))} \tag{3.74}$$

$$z_i(m) \equiv \left(\frac{q_i(m)}{q_R} \right)^2 \tag{3.75}$$

$$F_0(z) = 1 \tag{3.76}$$

$$F_1(z) = \sqrt{\frac{2z}{z+1}} \tag{3.77}$$

$$F_2(z) = \sqrt{\frac{13z^2}{(z-3)^2 + 9z}} \tag{3.78}$$

$$F_\ell(z) = \sqrt{\frac{\left| h_\ell^{(1)}(1) \right|^2}{z \left| h_\ell^{(1)}(\sqrt{z}) \right|^2}} \tag{3.79}$$

---

[5]Here, Γ depends on m, which is true for a relativistic form of the Breit-Wigner amplitude.
[6]However, $\gamma_{\alpha i}$ may itself be negative so long as it is purely real.

where $q_i(m) = m\rho_i(m)/2$ is the breakup momentum for the ith channel[7], q_R is the impact parameter/interaction radius (we use 0.1973 GeV in our calculations), and $h_\ell^{(1)}$ is a spherical Hankel function of the first kind (see Equation 2.4 of [66])

For clarity, we typically reparameterize these partial widths such that

$$g_{\alpha i}(m) = g_{\alpha i} B_{\alpha i}^\ell(m) \sqrt{\rho_i(m)} \tag{3.80}$$

so we can define the Lorentz-invariant K-matrix, $\hat{K}$, as

$$K_{ij}(m) = \sqrt{\rho_i(m)} \left(\sum_\alpha B_{\alpha i}^\ell(m) \left[\frac{g_{\alpha i} g_{\alpha j}}{m_\alpha^2 - m^2} + \sum_n \bar{c}_{nij} m^{2n} \right] B_{\alpha j}^\ell \right) \sqrt{\rho_j(m)}$$

$$K_{ij}(m) = \sqrt{\rho_i(m)} \hat{K}_{ij}(m) \sqrt{\rho_j(m)} \tag{3.81}$$

$$\tag{3.82}$$

where we have absorbed some multiplicative factors into c_{ij} to form the series expansion over powers of m^2 (since $\rho(m)$ and $B_{\alpha i}^\ell(m)$ only contain even powers of m) with coefficients $\bar{c}_{ij}$. Here, $\bar{K}$ replaces K in Equation (3.67) as an intermediate step to defining a Lorentz-invariant formulation.

According to Chung [59], the Lorentz-invariant form of the T-matrix, $\hat{T}$ can be written as

$$T = \sqrt{\rho} \hat{T} \sqrt{\rho} \tag{3.83}$$

where we define the notation

$$\rho_{ij}(m) \equiv \rho_i(m) \delta_{ij} \tag{3.84}$$

$$\sqrt{\rho_{ij}(m)} \equiv \sqrt{\rho_i(m)} \delta_{ij} \tag{3.85}$$

In terms of Equations (3.64), (3.67) and (3.82), we can write

$$\hat{K}^{-1} = \hat{T}^{-1} + \iota\rho \tag{3.86}$$

Following the previous derivation with these invariant forms, we find that

$$\hat{T} = (I - \iota\hat{K}\rho)^{-1}\hat{K} \tag{3.87}$$

---

[7]i.e. the magnitude of the momentum either decay product will have in the rest frame of the decay

Production Amplitudes from a K-Matrix

The T-matrix given in Equation (3.87) describes s-channel resonances (as in $a + b \to X \to c + d$). We can transform this into a production amplitude following Aitchison [67]:

$$\hat{F} = (I - \imath \hat{K}\rho)^{-1}\hat{P} \tag{3.88}$$

where

$$\hat{P}_i(\vec{\beta}; m) = \sum_\alpha \left(\frac{\beta_\alpha g_{\alpha i}}{m_\alpha^2 - m^2} + \sum_n c_{ni} m^{2n} \right) B_{\alpha i}^\ell(m) \tag{3.89}$$

Here, β_α describes the complex coupling from the initial state to the resonance α. This can be thought of like a coupling coefficient in front of a single Breit-Wigner. The polynomial of coefficients are included for completeness, as any constant terms in P preserve unitarity in the same way as constant terms in K, and the division of the factor of $\rho_i(m) \sim \rho_i(m^2)$ from Equation (3.80) and $B_{\alpha i}^\ell(m) \sim B_{\alpha i}^\ell(m^2)$ creates the given form.

The Chew-Mandelstam Matrix

For reasons which will become clear, we will define the diagonal matrix C, called the Chew-Mandelstam matrix, with the property

$$\mathrm{Im}[C(m)] = -\rho(m) \quad \text{or} \quad C(m) = A(m) - \imath\rho(m) \tag{3.90}$$

for some real function $A(m)$. It can be shown that we can replace $-\imath\rho$ in Equation (3.87) with such a matrix C and still retain a valid K-matrix representation [68],

$$\hat{T} = (I + \hat{K}C)^{-1}\hat{K} \tag{3.91}$$

and

$$\hat{F} = (I + \hat{K}C)^{-1}\hat{P} \tag{3.92}$$

The exact form of $A(m)$ is arbitrary, but we will be using

$$C_{ii}(m) = C((m_1 + m_2)^2) + \frac{\rho_i(m)}{\pi} \ln\left[\frac{\chi_i^+(m) + \rho_i(m)}{\chi_i^+(m) - \rho_i(m)} \right] - \frac{\chi_i^+(m)}{\pi} \frac{m_2 - m_1}{m_1 + m_2} \ln \frac{m_2}{m_1} \tag{3.93}$$

where m_1 and m_2 are the masses of the final state of the ith decay channel, and we can choose $C((m_1+m_2)^2) = 0$ for normalization. See [69], [70], [71], and [72] for derivations and additional details of this expression. The motivation for this choice is that it behaves better below threshold than $\rho(m)$, as can be seen in Figure 3.2.
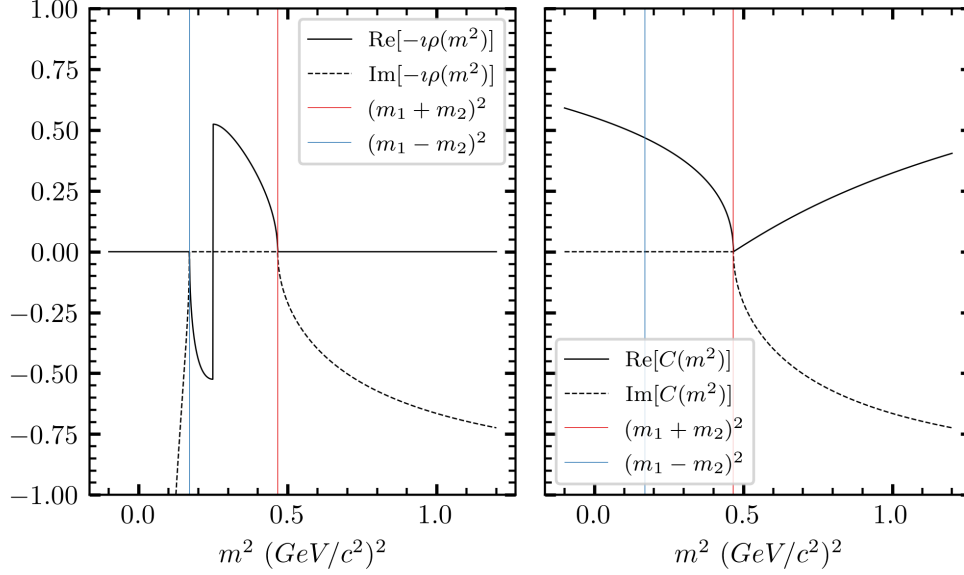
Figure 3.2: A comparison of the normal phase-space function, $\rho(m)$ (left) and the Chew-Mandelstam matrix, $C(m)$ (right) on the $\pi^0\eta$ channel. Both functions have the same imaginary part above the threshold $m = m_1 + m_2$, but phase-space function has a branch cut at $m^2 = \frac{(m_1^2 - m_2^2)^2}{m_1^2 + m_2^2}$ (the jump in the left plot between the red and blue lines) as well as a discontinuity at $m^2 = (m_1 - m_2)^2$ in both real and imaginary parts.

The impetus of this complication is that this particular formulation of the Chew-Mandelstam matrix is used in [73] and [74]. We do not have enough data to constrain the pole positions of every resonance in this channel (as we only have access to one of several channels used in those papers), so we will use the K-matrix coefficients ($g_{i\alpha}$ and m_α) from their coupled-channel analysis of data from the Crystal Barrel and COMPASS experiments as fixed values in our analysis, fitting only the couplings ($\vec{\beta}$) to photoproduction. Additionally, using the results from these papers requires a Adler zero term in front of the K-matrix for the f_0 mesons of the form $\frac{(s - s_0)}{s_{\text{norm}}}$, where they use $s_0 = m_{\pi_0}^2/2$ and $s_{\text{norm}} = 1$.

We can then combine Equation (3.92) with Equation (3.58), choosing $T_{M;\eta}^{J(\epsilon)}(\vec{\beta}; m) = \hat{F}(\vec{\beta}; m)$, to form a mass-dependent model of polarized photoproduction for the $K_S^0 K_S^0$ channel which will be further discussed in Section 4.3.

3.4 Waveset Selection

Chapter 4

Results and Systematic Studies

4.1 Fitting Methods

To fit the aforementioned models to the data, we employ an algorithm which maximizes the likelihood function,

$$\mathcal{L}(\vec{\beta}) = e^{-\mathcal{N}} \frac{\mathcal{N}^N}{N!} \prod_{i=1}^{N} \mathcal{P}_i(\vec{\beta}) \tag{4.1}$$

where N is the number of events in the data, $\mathcal{N}$ is the number of events predicted by the model, and $\mathcal{P}_i(\vec{\beta})$ is the normalized probability distribution function evaluated on the ith event at position $\vec{\beta}$ in parameter space. The term in front of the product is a Poisson distribution which describes the "extended" maximum likelihood method. We relate these probability distributions to our modeled intensity function in Equation (3.58) via the normalization,

$$\mathcal{I}(\vec{\beta}; m_i, s_i, \Omega_i, P_{\gamma,i}, \Phi_i) \equiv \mathcal{I}_i(\vec{\beta}) = \mathcal{N} \mathcal{P}_i(\vec{\beta}) \tag{4.2}$$

h

By absorbing the factor of $\mathcal{N}^N$ into the product, we find

$$\mathcal{L}(\vec{\beta}) = \frac{e^{-\mathcal{N}}}{N!} \prod_{i=1}^{N} \mathcal{I}_i(\vec{\beta}) \tag{4.3}$$

We want to maximize this function, but the product makes this computationally difficult and unstable, since it can grow very large (if $\mathcal{I} > 1$) or very small (if $\mathcal{I} < 1$) to a point where its value exceeds floating-point precision. The standard solution is to instead minimize the negative logarithm of the likelihood instead,

$$-2 \ln \mathcal{L}(\vec{\beta}) = -2 \left(\sum_{i=1}^{N} \left[\ln \mathcal{I}_i(\vec{\beta}) \right] - \mathcal{N} - \ln N! \right) \tag{4.4}$$

where the factor of two scales the log-likelihood to correspond to a χ^2 distribution as $N \rightarrow \infty$ by Wilks' theorem, allowing us to obtain an accurate covariance matrix from the fit for uncertainty estimation.

In an ideal world, we could stop here, ignoring the last two terms as they are constant in β and therefore do not contribute to the gradient of the negative log-likelihood. However, we must also consider the efficiency of the detector itself, which we will define as $\eta(m_i, s_i, \Omega_i, P_{\gamma,i}, \Phi_i) \equiv \eta_i$. In principle, we do not know the analytical form of this function, but we will later see that we can approximate it using Monte Carlo simulated data.

With this efficiency function in mind, we find that $\mathcal{N}$, the normalization factor which describes the number of events predicted by the model, becomes

$$\mathcal{N} = \int d\vec{x}\, \mathcal{I}(\vec{\beta};\vec{x})\eta(\vec{x}) \tag{4.5}$$

where $\vec{x} = (m, s, \Omega, P_\gamma, \Phi)$. This means we can write the normalized probability distribution functions as

$$\mathcal{P}_i(\vec{\beta}) = \frac{1}{\mathcal{N}}\mathcal{I}_i(\vec{\beta})\eta_i \tag{4.6}$$

This changes the negative log-likelihood to

$$-2\ln\mathcal{L}(\vec{\beta}) = -2\left(\sum_{i=1}^{N}\left[\ln\mathcal{I}_i(\vec{\beta})\right] - \int d\vec{x}\,\mathcal{I}(\vec{\beta};\vec{x})\eta(\vec{x}) - \ln N! + \sum_{i=1}^{N}\left[\ln\eta_i\right] \right) \tag{4.7}$$

$$= -2\left(\sum_{i=1}^{N}\left[\ln\mathcal{I}_i(\vec{\beta})\right] - \int d\vec{x}\,\mathcal{I}(\vec{\beta};\vec{x})\eta(\vec{x}) \right) + C \tag{4.8}$$

Next, we need a way of dealing with the integral term, particularly with the $\eta(\vec{x})$ function for which we do not have access to the analytical form. To approximate this integral, we use both the fundamental theorem of calculus and the mean value theorem for derivatives, which together relate the integral of a function to its average value on the domain of integration,

$$\int_{\mathbb{D}} f(\vec{x})\, d\vec{x} = \mathbb{A}\left\langle f(\vec{x})\right\rangle \tag{4.9}$$

where $\mathbb{A}$ is the area of the integration domain $\mathbb{D}$ and $\left\langle f(\vec{x})\right\rangle$ denotes the average value of $f(\vec{x})$ on that domain. If we generate phase-space Monte Carlo for the $K_S^0 K_S^0$ channel, we can model $\eta(\vec{x})$ as an indicator function corresponding to whether or not an event is detected by a simulation of the detector, passes through the reconstruction process described in Section 2.1, and passes through our finer data selection from Section 2.2. We can then write the average as a sum over the "accepted" Monte Carlo events,

$$\int d\vec{x}\,\mathcal{I}(\vec{\beta};\vec{x})\eta(\vec{x}) = \frac{1}{\mathbb{A}N_g}\sum_{j=1}^{N_a}\left[\mathcal{I}_j(\vec{\beta})\right] \tag{4.10}$$

where $\mathcal{I}_j(\vec{\beta})$ is evaluated on the jth accepted Monte Carlo event[1], and N_a and N_g are the number of accepted and generated events, respectively. We still need to deal with the factor of $\mathbb{A}$. We could absorb this into our intensity function by scaling the intensity by $\mathbb{A}^{N_a}$, which would eliminate it from this term. In the data term, we would then have

$$\sum_{i=1}^{N} \left[\mathbb{A}^{N_a} \mathcal{I}_i(\vec{\beta}) \right] = \sum_{i=1}^{N} \left[\mathcal{I}_i(\vec{\beta}) \right] + N N_a \ln \mathbb{A} \tag{4.11}$$

where the new additive term is constant in $\vec{\beta}$ and can again be ignored in the minimization. At this stage, we need to minimize

$$-2 \ln \mathcal{L}(\vec{\beta}) = -2 \left(\sum_{i=1}^{N} \left[\ln \mathcal{I}_i(\vec{\beta}) \right] - \frac{1}{N_g} \sum_{i=j}^{N_a} \left[\mathcal{I}_j(\vec{\beta}) \right] \right) \tag{4.12}$$

We can incorporate event weights (from accidental subtraction or sPlot, for example) into these sums as

$$-2 \ln \mathcal{L}(\vec{\beta}) = -2 \left(\sum_{i=1}^{N} \left[w_i \ln \mathcal{I}_i(\vec{\beta}) \right] - \frac{1}{N_g} \sum_{i=j}^{N_a} \left[w_j \mathcal{I}_j(\vec{\beta}) \right] \right) \tag{4.13}$$

An additional scaling of the intensity with $\mathcal{I}(\vec{\beta}) \to \varepsilon^{-N_\alpha} \mathcal{I}(\vec{\beta})$ with $N_g = \varepsilon N_a$ can be made to eliminate N_g from this expression, which adds a constant factor of $-N N_a \ln \varepsilon$ to the negative log-likelihood. This choice is optional, but it can be helpful from a computational/organizational standpoint when it comes to projecting the fitted model back onto each Monte Carlo dataset and is chosen in this analysis to give us

$$-2 \ln \mathcal{L}(\vec{\beta}) = -2 \left(\sum_{i=1}^{N} \left[w_i \ln \mathcal{I}_i(\vec{\beta}) \right] - \frac{1}{N_a} \sum_{i=j}^{N_a} \left[w_j \mathcal{I}_j(\vec{\beta}) \right] \right) \tag{4.14}$$

We can now choose a minimization algorithm to fit our data to various models which will be described in detail in Sections 4.2 and 4.3. For this analysis, fits were performed with `laddu`, an amplitude analysis engine I wrote, which uses the L-BFGS-B minimization algorithm, a memory-efficient variant of the Broyden-Fletcher-Goldfarb-Shanno algorithm which allows for box constraints on the parameter space [75].

To obtain plots of the fitted model, we can weight each event in either the accepted or generated Monte Carlo (for results without and with efficiency correction, respectively) as follows,

$$\hat{w}_j = \frac{w_j \mathcal{I}_j(\vec{\beta}^*)}{N_{\text{MC}}} \tag{4.15}$$

where $\vec{\beta}^*$ is the value of the fit parameters which maximizes the likelihood and N_{MC} is N_a or N_g depending on which set of Monte Carlo we are using. We can additionally isolate individual waves by manually setting the coefficients of other waves to zero before evaluating the intensity.

---

[1]This is not to be confused with $\mathcal{I}_i(\vec{\beta})$, which we will use to refer to the function evaluated over data. These terms will always stay in separate sums for clarity.

Uncertainty Estimation

Quasi-Newton minimization algorithms like L-BFGS-B[2] perform gradient descent by making progressively better estimations of the Hessian matrix $\mathbf{H}$ at each step in the algorithm. One can then obtain an estimate of the uncertainty of the ith parameter from $\sigma_i = \sqrt{(\mathbf{H}^{-1})_{ii}}$, for which we can either use the Hessian approximate at the end of the minimization or calculate the true Hessian to some arbitrary level of computational precision using finite differences. This gives us the uncertainty on each fit parameter, but not the uncertainty on the number of modeled counts in a particular bin. Propagating the uncertainty is straightforward mathematically, but complicated computationally. Additionally, the Hessian method does not give us any further detail about the shape of the likelihood surface at the minimum other than the standard deviation of a particular parameter. To examine higher order moments, we require methods which either directly sample the parameter space, e.g. Markov chain Monte Carlo (MCMC), or which resample the data, e.g. the jackknife or bootstrap methods. For this thesis, we will use the bootstrap, as MCMC methods are much more time-consuming and require the tuning of hyperparameters and walker steps, and the jackknife method, which involves resampling the data by omitting one or more events at a time, is only preferred when the bootstrap method described as follows is computationally infeasible.

The bootstrap method derives from the following reasoning. If we had some existing estimate of uncertainty, we could check the estimate by simply collecting more data, performing the analysis on this new data, and observing if our results fall within the estimated uncertainty. However, even if we were to obtain more data, we lack the original estimate of uncertainty. We can obtain such an estimate by "pulling ourselves up by our bootstraps" and resampling the data with replacement to obtain a slightly different "bootstrapped" dataset, which has the same number of events as the original, but contains some duplicate events and misses some of the original events. Assuming the original data is a representative sample of our population (in this case, assuming a new set of data would only effect the precision of our results), we can obtain several of these bootstrapped datasets and perform our fit. We must start each fit at the true minimum found from the original dataset, since we want to understand the uncertainty as it relates to our model, not to the path the minimizer takes, which may run into different local/false minima in each bootstrapped dataset. The distribution of a parameter over many bootstrapped analyses can then be associated with the uncertainty of that parameter.

We begin by defining the statistic $\hat{\beta}_i(X) = \beta_i^*$ where X represents the dataset and $\hat{\beta}_i$ is the maximum likelihood estimator of β_i which maps the events in the dataset to a particular value β_i^* via the fitting process we described in Section 4.1. We then resample the data with replacement B times to obtain bootstrapped datasets $\{X_1, \dots, X_b\}$. The standard error on the parameter β_i is then given by [76],

---

[2]This also applies to other algorithms commonly used in this field, like `MINUIT`

$$\hat{\sigma}_{\beta_i}^{(B)} = \sqrt{\sum_{b=1}^{B} \frac{\left(\hat{\beta}_i(X_b) - \frac{1}{B} \sum_{b'=1}^{B} \hat{\beta}_i(X_{b'}) \right)^2}{B-1}} \tag{4.16}$$

We can also extract confidence intervals for each parameter using bootstrapping. These might be more useful than our standard error estimates, since the shape of the likelihood surface is not necessarily symmetric. First, we define the cumulative distribution function of the $\hat{\beta}_i$ statistic as [76],

$$\hat{\text{CDF}}_i(t) = \Pr\left(\hat{\beta}_i < t \right) = \frac{\#\left\{ \hat{\beta}_i(X_b) < t \right\}}{B} \tag{4.17}$$

where #{·} represents the number of values satisfying the enclosed condition[3]. Then, for some value $\alpha \in [0, 1]$, we define

$$\hat{\theta}_i(\alpha) \equiv \hat{\text{CDF}}_i^{-1}(\alpha) \tag{4.18}$$

We then define the $(1 - 2\alpha) \cdot 100\%$ central confidence interval for β_i as $\beta_i \in [\hat{\theta}(\alpha), \hat{\theta}(1 - \alpha)]$. Furthermore, we can can define a bias-corrected confidence interval [76] which corrects for the fact that the mean of the bootstrap distribution is not necessarily the value obtained from the fit to the original data. First, we define a bias-correction factor,

$$z_0 = \Phi^{-1}\left(\hat{\text{CDF}}_i(\hat{\beta}_i(X)) \right) \tag{4.19}$$

where $\Phi(z)$ is the cumulative distribution function of the standard normal distribution and $\hat{\beta}_i(X)$ is the value of β_i we obtain from the fit to the original dataset X. Then, the bias-corrected $(1 - 2\alpha) \cdot 100\%$ central confidence interval is $\beta_i \in \left[\hat{\theta}(\alpha_{\text{lo}}), \hat{\theta}(\alpha_{\text{hi}}) \right]$ where

$$\alpha_{\text{lo}} = \Phi\left(2z_0 + z(\alpha) \right) \tag{4.20}$$

$$\alpha_{\text{hi}} = \Phi\left(2z_0 + z(1 - \alpha) \right) \tag{4.21}$$

$$z(\alpha) \equiv \Phi^{-1}(\alpha) \tag{4.22}$$

The interpretation of a confidence interval obtained this way is frequentist: If we were to repeat the GlueX experiment many times and evaluated β_i for each experiment, we would expect $P\%$ of the values to fall within an $P\%$ confidence interval. The Bayesian approach would be to assign a "credible interval", where the probability that an estimate falls in the credible interval is $P\%$.

---

[3]The last equality here only holds in the limit as $B \to \infty$, but we will ignore this for now.

4.2 Mass-Independent Fits

4.3 Mass-Dependent Fits

Guided Fits

4.4 Systematics

Chapter 5

Conclusion

Bibliography

[1]   W. D. Ross, "Aristotle's metaphysics. a revised text with introduction and commentary," vol. 34, pp. 351–361, 135 1925.

[2]   R. P. Hardie and R. K. Gaye, "Physics," in *Complete Works of Aristotle, Volume 1: The Revised Oxford Translation*, J. Barnes, Ed. Princeton University Press, 1984.

[3]   J. Dalton, *A New System of Chemical Philosophy*. Manchester: Printed by S. Russell for R. Bickerstaff, Strand, London, 1808, p. 248.

[4]   J. J. Thomson, "Cathode rays," vol. 44, pp. 293–316, 1897.

[5]   J. J. Thomson, *The Corpuscular Theory of Matter*. Scribner's Sons, New York, 1907.

[6]   E. Rutherford, "Lxxix. the scattering of α and β particles by matter and the structure of the atom," vol. 21, pp. 669–688, 125 1911, ISSN: 1941-5982. DOI: 10.1080/14786440508637080.

[7]   O. Masson, "Xxiv. the constitution of atoms," vol. 41, pp. 281–285, 242 1921, ISSN: 1941-5982. DOI: 10.1080/14786442108636219.

[8]   J. Chadwick, "Possible existence of a neutron," vol. 129, p. 312, 3252 1932, ISSN: 1476-4687. DOI: 10.1038/129312a0.

[9]   M. Gell-Mann, "A schematic model of baryons and mesons," vol. 8, pp. 214–215, 3 1964, ISSN: 0031-9163. DOI: 10.1016/S0031-9163(64)92001-3.

[10] G. Aad et al., "Observation of a new particle in the search for the standard model higgs boson with the atlas detector at the lhc," vol. 716, pp. 1–29, 1 2012, ISSN: 0370-2693. DOI: 10.1016/j.physletb.2012.08.020.

[11] K. G. Wilson, "Confinement of quarks," vol. 10, pp. 2445–2459, 8 1974. DOI: 10.1103/PhysRevD.10.2445.

[12] C. J. Morningstar and M. Peardon, "Glueball spectrum from an anisotropic lattice study," vol. 60, p. 034 509, 3 1999, ISSN: 0556-2821, 1089-4918. DOI: 10.1103/PhysRevD.60.034509.

[13]   P. A. Zyla et al., "Review of particle physics," vol. 2020, p. 083C01, 8 2020, ISSN: 2050-3911. DOI: 10.1093/
       ptep/ptaa104.

[14]   S. Adhikari et al., "The gluex beamline and detector," vol. 987, p. 164 807, 2021, ISSN: 01689002. DOI: 10.1016/
       j.nima.2020.164807.

[15]   M. Acciarri et al., "$K_S^0 K_S^0$ final state in two-photon collisions and implications for glueballs," vol. 501, pp. 173–
       182, 3 2001, ISSN: 0370-2693. DOI: 10.1016/S0370-2693(01)00116-2.

[16]   V. Mathieu, N. Kochelev, and V. Vento, "The physics of glueballs," vol. 18, pp. 1–49, 01 2009, ISSN: 0218-3013.
       DOI: 10.1142/S0218301309012124.

[17]   S. Chandavar et al., "Double K_S^0 photoproduction off the proton at clas," vol. 97, p. 025 203, 2 2018. DOI: 10.
       1103/PhysRevC.97.025203.

[18]   M. D. Corato et al., "V^0 pairs produced in the ecole polytechnique one meter propane bubble chamber by π^-
       of 6, 1, 11, 6 and 18, 1 gev/c," in Conférence Internationale d'Aix-en-Provence sur les Particules Elémentaires, E.
       Crémieu-Alcan, P. Falk-Vairant, and O. Lebey, Eds., Sep. 1961, pp. 101–110.

[19]   A. R. Erwin, G. A. Hoyer, R. H. March, W. D. Walker, and T. P. Wangler, "Experimental cross section for
       $\pi\pi \rightarrow K\bar{K}$," vol. 9, pp. 34–36, 1 1962. DOI: 10.1103/PhysRevLett.9.34.

[20]   G. Alexander et al., "Final-state interactions in the $\pi^- p \rightarrow K + \bar{K} + N$ reaction," vol. 9, pp. 460–464, 11 1962.
       DOI: 10.1103/PhysRevLett.9.460.

[21]   D. J. Crennell et al., "Observation of an enhancement in the $I = 0$ $K_1^0 K_1^0$ system at 1068 mev," vol. 16, pp. 1025–
       1029, 22 1966. DOI: 10.1103/PhysRevLett.16.1025.

[22]   R. I. Hess, O. I. Dahl, L. M. Hardy, J. Kirz, and D. H. Miller, "Low-mass $K\overline{K}$ systems produced in $\pi^- p$ interactions
       below 5 bev/c," vol. 17, pp. 1109–1112, 21 1966. DOI: 10.1103/PhysRevLett.17.1109.

[23]   O. I. Dahl, L. M. Hardy, R. I. Hess, J. Kirz, and D. H. Miller, "Strange-particle production in $\pi^- p$ interactions
       from 1.5 to 4.2 bev/c. in three-and-more-body final states," vol. 163, pp. 1377–1429, 5 1967. DOI: 10.1103/
       PhysRev.163.1377.

[24]   W. Beusch et al., "Observation of resonance in the $K_0^1 K_0^1$ system," vol. 25, pp. 357–361, 5 1967, ISSN: 0370-2693.
       DOI: 10.1016/0370-2693(67)90095-0.

[25]   T. F. Hoang et al., "$K_1^0 K_1^0$ threshold enhancement in $\pi^- p \rightarrow K_1^0 K_1^0 n$ at 4 and 5 gev/c," vol. 21, pp. 316–319, 5
       1968. DOI: 10.1103/PhysRevLett.21.316.

[26]   T. F. Hoang et al., "Investigation of $\pi^- p \rightarrow K_1^0 K_1^0 n$ at 4 and 5 gev/c," vol. 184, pp. 1363–1374, 5 1969. DOI:
       10.1103/PhysRev.184.1363.

[27] W. Beusch, A. Birman, D. Websdale, and W. Wetzel, "A new upper limit for the decay rate $\Gamma(f' \to \pi\pi)$," vol. 60, pp. 101–104, 1 1975, ISSN: 0370-2693. DOI: 10.1016/0370-2693(75)90539-0.

[28] W. Wetzel et al., "A study of $\pi\pi \to KK$ using an experiment on $\pi^- p \to K_S^0 K_S^0 n$ at 8.9 gev/c," vol. 115, pp. 208–236, 2 1976, ISSN: 0550-3213. DOI: 10.1016/0550-3213(76)90254-6.

[29] N. M. Cason et al., "Observation of a new scalar meson," vol. 36, pp. 1485–1488, 25 1976. DOI: 10.1103/PhysRevLett.36.1485.

[30] V. A. Polychronakos et al., "Study of the reaction $\pi^- p \to n K_S^0 K_S^0$ at 6.0 and 7.0 gev/c," vol. 19, pp. 1317–1335, 5 1979. DOI: 10.1103/PhysRevD.19.1317.

[31] F. Barreiro et al., "Production and decay properties of $f'(1514)$ in $K^- p$ interactions at 4.2 gev/c," vol. 121, pp. 237–250, 2 1977, ISSN: 0550-3213. DOI: 10.1016/0550-3213(77)90436-9.

[32] S. R. Gottesman et al., "Peripheral production and decay of $K_S^0 K_S^0$ in the reaction $\pi^- p \to K_S^0 K_S^0$ + neutrals at 15.4 gev/c," vol. 22, pp. 1503–1512, 7 1980. DOI: 10.1103/PhysRevD.22.1503.

[33] A. Etkin et al., "Amplitude analysis of the $K_S^0 K_S^0$ system produced in the reaction $\pi^- p \to K_S^0 K_S^0 n$ at 23 gev/c," vol. 25, pp. 1786–1802, 7 1982. DOI: 10.1103/PhysRevD.25.1786.

[34] M. Althoff et al., "Production of KK-pairs in photon-photon collisions and the excitation of the tensor meson $f'(1515)$," vol. 121, pp. 216–222, 2 1983, ISSN: 0370-2693. DOI: 10.1016/0370-2693(83)90917-6.

[35] R. S. Longacre et al., "A measurement of $\pi^- p \to K_S^0 K_S^0 n$ at 22 gev/c and a systematic study of the 2^{++} meson spectrum," vol. 177, pp. 223–227, 2 1986, ISSN: 0370-2693. DOI: 10.1016/0370-2693(86)91061-0.

[36] C. Berger et al., "Tensor meson excitation in the reaction $\gamma\gamma \to K_S^0 K_S^0$," vol. 37, pp. 329–335, 3 1988, ISSN: 1431-5858. DOI: 10.1007/BF01578125.

[37] D. Aston et al., "A study of the $K_S^0 K_S^0$ system in the reaction $K^- p \to K_S^0 K_S^0 \Lambda$ at 11 gev/c," vol. 301, pp. 525–553, 4 1988, ISSN: 0550-3213. DOI: 10.1016/0550-3213(88)90276-3.

[38] H. .-. Behrend et al., "The $K_S^0 K_S^0$ final state in $\gamma\gamma$ interactions," vol. 43, pp. 91–96, 1 1989, ISSN: 1431-5858. DOI: 10.1007/BF02430613.

[39] M. Acciarri et al., "Study of the $K_S^0 K_S^0$ final state in two-photon collisions," vol. 363, pp. 118–126, 1 1995, ISSN: 0370-2693. DOI: 10.1016/0370-2693(95)01041-N.

[40] M. A. Reyes et al., "Partial wave analysis of the centrally produced $K_S K_S$ system at $800 GeV/c$," vol. 81, pp. 4079–4082, 19 1998. DOI: 10.1103/PhysRevLett.81.4079.

[41] B. P. Barkov et al., "Discovery of a narrow resonance state of the system $K_S K_S$ at mass 1520 mev," vol. 70, pp. 248–253, 4 1999, ISSN: 1090-6487. DOI: 10.1134/1.568160.

[42] G. D. Tikhomirov, I. A. Erofeev, O. N. Erofeeva, and V. N. Luzin, "Resonances in the $K_S K_S K_L$ system produced in collisions of negative pions with a carbon target at a momentum of 40 gev," vol. 66, pp. 828–835, 5 2003, ISSN: 1562-692X. DOI: 10.1134/1.1576456.

[43] V. A. Schegelsky, A. V. Sarantsev, V. A. Nikonov, and A. V. Anisovich, "The $K_S^0 K_S^0$ final state in two-photon collisions and $SU(3)$ tensor nonets," vol. 27, pp. 207–212, 2 2006, ISSN: 1434-601X. DOI: 10.1140/epja/i2005-10264-2.

[44] V. V. Vladimirsky et al., "Analysis of the $K_S K_S$ system from the reaction $\pi^- p \to K_S K_S n$ at 40 gev," vol. 69, pp. 493–509, 3 2006, ISSN: 1562-692X. DOI: 10.1134/S1063778806030124.

[45] S. Uehara et al., "High-statistics study of K_S^0 pair production in two-photon collisions," vol. 2013, p. 123C01, 12 2013, ISSN: 2050-3911. DOI: 10.1093/ptep/ptt097.

[46] A. Ali et al., "Installation and commissioning of the gluex dirc," vol. 15, p. C09010, 09 2020, ISSN: 1748-0221. DOI: 10.1088/1748-0221/15/09/C09010.

[47] C. Bierlich et al., "A comprehensive guide to the physics and usage of pythia 8.3," 2022. DOI: 10.48550/arXiv.2203.11601.

[48] J. Allison et al., "Geant4 developments and applications," vol. 53, pp. 270–278, 1 2006, ISSN: 1558-1578. DOI: 10.1109/TNS.2006.869826.

[49] J. Allison et al., "Recent developments in geant4," vol. 835, pp. 186–225, 2016, ISSN: 0168-9002. DOI: 10.1016/j.nima.2016.06.125.

[50] S. Agostinelli et al., "Geant4—a simulation toolkit," vol. 506, pp. 250–303, 3 2003, ISSN: 0168-9002. DOI: 10.1016/S0168-9002(03)01368-8.

[51] C. S. Peirce, "The numerical measure of the success of predictions," vol. ns-4, pp. 453–454, 93 1884, ISSN: 0036-8075, 1095-9203. DOI: 10.1126/science.ns-4.93.453.b.

[52] W. J. Youden, "Index for rating diagnostic tests," vol. 3, pp. 32–35, 1 1950, ISSN: 1097-0142. DOI: 10.1002/1097-0142(1950)3:1<32::AID-CNCR2820030106>3.0.CO;2-3.

[53] E. F. Schisterman, N. J. Perkins, A. Liu, and H. Bondell, "Optimal cut-point and its corresponding youden index to discriminate individuals using pooled blood samples," vol. 16, p. 73, 1 2005, ISSN: 1044-3983. DOI: 10.1097/01.ede.0000147512.81966.ba.

[54] D. M. W. Powers, "Evaluation: From precision, recall and f-measure to roc, informedness, markedness and correlation," 2020. DOI: 10.48550/ARXIV.2010.16061.

[55] M. Pivk and F. R. L. Diberder, "Splot: A statistical tool to unfold data distributions," vol. 555, pp. 356–369, 1-2 2005, ISSN: 01689002. DOI: 10.1016/j.nima.2005.08.106.

[56] H. Dembinski, M. Kenzie, C. Langenbruch, and M. Schmelling, "Custom orthogonal weight functions (cows) for event classification," vol. 1040, p. 167 270, 2022, ISSN: 01689002. DOI: 10.1016/j.nima.2022.167270.

[57] H. Akaike, "Information theory and an extension of the maximum likelihood principle," in *Selected Papers of Hirotugu Akaike*, E. Parzen, K. Tanabe, and G. Kitagawa, Eds. Springer, 1998, pp. 199–213, ISBN: 978-1-4612-1694-0.

[58] G. Schwarz, "Estimating the dimension of a model," vol. 6, pp. 461–464, 2 1978, ISSN: 0090-5364, 2168-8966. DOI: 10.1214/aos/1176344136.

[59] S. U. Chung, *Spin formalisms*, 1971. DOI: 10.5170/CERN-1971-008.

[60] J. D. Richman, "An experimenter's guide to the helicity formalism," CALT-68-1148, Tech. Rep., 1984.

[61] V. Mathieu et al., "Moments of angular distribution and beam asymmetries in $\eta\pi^0$ photoproduction at gluex," vol. 100, p. 054 017, 5 2019, ISSN: 2470-0010, 2470-0029. DOI: 10.1103/PhysRevD.100.054017.

[62] G. Breit and E. Wigner, "Capture of slow neutrons," vol. 49, pp. 519–531, 7 1936. DOI: 10.1103/PhysRev.49.519.

[63] S. U. Chung, J. Brose, R. Hackmann, E. Klempt, S. Spanier, and C. Strassburger, "Partial wave analysis in k-matrix formalism," vol. 507, pp. 404–430, 5 1995, ISSN: 1521-3889. DOI: 10.1002/andp.19955070504.

[64] K. L. Au, D. Morgan, and M. R. Pennington, "Meson dynamics beyond the quark model: Study of final-state interactions," vol. 35, pp. 1633–1664, 5 1987. DOI: 10.1103/PhysRevD.35.1633.

[65] J. M. Blatt and V. F. Weisskopf, *Theoretical Nuclear Physics.* Springer New York, 1979, ISBN: 978-1-4612-9961-5 978-1-4612-9959-2.

[66] F. von Hippel and C. Quigg, "Centrifugal-barrier effects in resonance partial decay widths, shapes, and production amplitudes," vol. 5, pp. 624–638, 3 1972. DOI: 10.1103/PhysRevD.5.624.

[67] I. J. R. Aitchison, "The *K*-matrix formalism for overlapping resonances," vol. 189, pp. 417–423, 2 1972, ISSN: 0375-9474. DOI: 10.1016/0375-9474(72)90305-3.

[68] D. J. Wilson, J. J. Dudek, R. G. Edwards, and C. E. Thomas, "Resonances in coupled $\pi K, \eta K$ scattering from lattice qcd," vol. 91, p. 054 008, 5 2015. DOI: 10.1103/PhysRevD.91.054008.

[69] J. A. Oller and E. Oset, "N/D description of two meson amplitudes and chiral symmetry," vol. 60, p. 074 023, 7 1999. DOI: 10.1103/PhysRevD.60.074023.

[70] J. L. Basdevant and E. L. Berger, "Unitary coupled-channel analysis of diffractive production of the A_1 resonance," vol. 16, pp. 657–678, 3 1977. DOI: 10.1103/PhysRevD.16.657.

[71]   J. A. Oller and U.-G. Meißner, "Chiral dynamics in the presence of bound states: Kaon–nucleon interactions revisited," vol. 500, pp. 263–272, 3 2001, ISSN: 0370-2693. DOI: 10.1016/S0370-2693(01)00078-8.

[72]   J. H. Reid and N. N. Trofimenkoff, "A generating function for chew–mandelstam functions," vol. 25, pp. 3540–3544, 12 1984, ISSN: 0022-2488. DOI: 10.1063/1.526093.

[73]   M. Albrecht et al., "Coupled channel analysis of $\bar{p}p \to \pi^0\pi^0\eta$, $\pi^0\eta\eta$ and $K^+K^-\pi^0$ at 900 mev/c and of $\pi\pi$-scattering data," vol. 80, p. 453, 5 2020, ISSN: 1434-6052. DOI: 10.1140/epjc/s10052-020-7930-x.

[74]   B. Kopf et al., "Investigation of the lightest hybrid meson candidate with a coupled-channel analysis of $\bar{p}p$-, π^-p- and $\pi\pi$-data," vol. 81, p. 1056, 12 2021, ISSN: 1434-6052. DOI: 10.1140/epjc/s10052-021-09821-2.

[75]   R. H. Byrd, P. Lu, J. Nocedal, and C. Zhu, "A limited memory algorithm for bound constrained optimization," vol. 16, pp. 1190–1208, 5 1995, ISSN: 1064-8275. DOI: 10.1137/0916069.

[76]   B. Efron, "Nonparametric standard errors and confidence intervals," vol. 9, pp. 139–158, 2 1981, ISSN: 1708-945X. DOI: 10.2307/3314608.